LIGHT SCATTERING FROM CORE-SHELL NANO-STRUCTURES: STRUCTURAL COLORATION

A THESIS

SUBMITTED TO THE DEPARTMENT OF PHYSICS

AND THE GRADUATE SCHOOL OF ENGINEERING AND SCIENCE

OF BILKENT UNIVERSITY

IN PARTIAL FULFILLMENT OF THE REQUIREMENTS

FOR THE DEGREE OF

MASTER OF SCIENCE

By

Muhammet Halit DOLAŞ

August, 2013

I certify that I have read this thesis and that in my opinion it is fully adequate, in scope and in quality, as a thesis for the degree of Master of Science.

Assoc. Prof. Dr. Mehmet Bayındır (Advisor)

I certify that I have read this thesis and that in my opinion it is fully adequate, in scope and in quality, as a thesis for the degree of Master of Science.

Assist. Prof. Dr. Necmi Bıyıklı

I certify that I have read this thesis and that in my opinion it is fully adequate, in scope and in quality, as a thesis for the degree of Master of Science.

Assoc. Prof. Dr. Fatih Danışman

Approved for the Graduate School of Engineering and Science:

Prof. Dr. Levent Onural
Director of the Graduate School

ABSTRACT

LIGHT SCATTERING FROM CORE-SHELL NANO-STRUCTURES: STRUCTURAL COLORATION

Muhammet Halit DOLAŞ
M.S. in Physics
Supervisor: Assoc. Prof. Dr. Mehmet Bayındır
August, 2013

In this work, we produced kilometer-long semiconducting cylindrical nano-structures by using a top-to-bottom nano-fabrication technique which was recently developed in our research group. Comparison of commonly used methods of producing nano-structures such as electrospinning and nano-imprint lithography versus iterative thermal size reduction (ISR) is done in terms of uniformity, geometry control, multi-material compatibility, yield and device integrability. While the others cannot fulfil all requirements, ISR shows impressive results in all aspects.

From very beginning to end, all steps of production and characterization of nano-wires produced by ISR, the design, chalcogenide glass production, preform preparation, fiber drawing, iterative size reduction, chemical etching and imaging are explained in details. In addition, production and characterization of nano-spheres by in-fiber fluid instability which is based on Plateau-Rayleigh instability is also demonstrated.

Theoretical study on scattering from small particles, Mie scattering, which is one of the mechanisms for structural coloration together with thin film interference, multilayer interference, diffraction grating and photonic crystals is done. Structural coloration due to scattering from small particles is simulated using Finite Domain Time Difference (FDTD) method and compared with theoretical results estimated for nano-wire and nano-sphere cases. Results are confirmed with observation of structural coloration by taking dark field optical microscopy images of the final products of ISR and in-fiber fluid instability processes.

Keywords: Nanotechnology, Fiber drawing, Nanostructures, Structural coloration, Mie scattering.

ÖZET

IŞIĞIN ÇİFT KATMANLI NANO YAPILARDAN SAÇILIMI: YAPISAL RENKLENME

Muhammet Halit DOLAŞ
Fizik, Yüksek Lisans
Tez Yöneticisi: Assoc. Prof. Dr. Mehmet Bayındır
Ağustos, 2013

Bu çalşmada kilometrelerce uzunlukta silindirik nano yaplar araştrma grubumuzca geliştirilen yeni bir yöntemle elde edildi. Günümüzdeki en iyi nano-tel üretim yöntemleri olan electrospinning ve nano baskı yöntemleri ile çalışmalarımızda kullandığımız tekrarlamalı boyut azaltma tekniği, düzenli üretim, boyut kontrolü, iki veya daha çok maddenin beraber kullanılabilmesi, üretim miktarı ve cihazlarla beraber çalışabilme başlıkları altında karşılaştırıldı. Diğer teknikler tüm branşlar söz konusu olduğunda gerekli performansı sağlayamazken tekrarlamalı boyut azaltma tekniği her açıdan etkileyici sonuçlar verdi.

En başından son aşamasına kadar, dizayn, çalkojen cam üretimi, başlangıç formunun hazırlanması, fiber çekimi, tekrarlamalı boyut azaltma, kimyasal çözümleme ve sonuçların görsel olarak yayınlanması gibi bütün nano-tel üretim ve karakterizasyon aşamaları, Plateau-Rayleigh kararsızlığına dayalı fiber içi sıvı kararsızlığı yöntemi ile elde edilmiş nano-kürelerin üretim ve karakterizasyon aşamaları ile baraber geniş olarak açıklandı.

İnce film kaplamalarından saçılım, iki veya daha fazla madde ile yapılan kaplamalardan saçılım, saçılım ızgarası ve fotonik kristal yöntemleri ile beraber yapısal renklenmenin sebeplerinden biri olan küçük partiküllerden saçılım olayı teorik açıdan incelendi. Nano-tel ve nano-küre durumları için küçük partiküllerden saçılım yöntemi ile oluşan yapısal renklenme FDTD (sınırlı alan zaman farkı) metodu ile simüle edildi ve sonuçlar MATLAB ile hesaplanan teorik sonuçlarla karşılaştırıldı. Tekrarlamalı boyut azaltma yöntemi ile elde edilmiş nano-tel ve nano-kürelerdeki yapısal renklenme optik mikroskop yardımı ile görüntülendi.

Anahtar sözcükler: Nanoteknoloji, Fiber, Nano yapılar, Yapısal renklenme.

Acknowledgement

I would like to thank my advisor Assoc. Prof. Dr. Mehmet Bayındır, my seniors Assist. Prof. Dr. Mecit Yaman, Mehmet Kanık, Dr. Tural Khudiyev and Murat Dere my friend Muhammet Çelebi and all members of Bayindir Researh Group for their assistance and to my family for their support.

Financial support form TUBİTAK (The Scientific and Technological Research Council of Turkey) is also gratefully acknowledged.

Contents

List of Figures

List of Tables

Chapter 1

Introduction

Colors, arguably the most appealing perfection of nature, the basic cause and an exciting result of complex structure of human eye, the precious ingredient almost for all kind of arts are appreciated, wondered, discovered by ages. Elements that cause coloration become clearer with the discovery of absorbtion and scattering of light [1]. Not only nonuniform absorbtion for different wavelengths of light by dyes or pigments [2] [3] but also scattering of light from periodic or quasi periodic structures cause coloration i.e. structural coloration [4] [5] [6] [7]. Thin film interference, multilayer interference, diffraction gratings, phonic crystals and scattering from small particles of sizes comparable to wavelength of light are main causes for the structural coloration [8] [9] [10] [11]. Although it is not as perfect as nature, scientists can mimic such structural coloration mechanisms with recently growing nano-scaled production technologies.

Although in this work we are aiming to observe structural coloration in nano-scale dielectric materials, light-matter interactions for non-metallic materials at nano-scale sizes are bound by diffraction limit which is equal to half of the wavelength of light, the minimum size of the material at which it can affect light [12] [13]. However, in terms of dielectric materials, absorption and scattering by small particles that results leaky-mode resonances in the domain of Lorenz-Mie theory can overcome diffraction limit problem [14]. Also using dielectrics in nano-structured arrays that can be characterized by an effective medium models

[15] or producing dielectrics as periodic structures showing photonic crystal effect [16] can overcome diffraction limit problem. Guiding light inside a high refractive index dielectric material at specific wavelength [17] and multiple scattering phenomenon [18] is also possible for optical usage of dielectrics.

Recent top-down [19] [20] [21] and bottom-up [22] [23] [24] production methods for nano-structures allow production of functional nano-scaled structures [25]. However, these methods, even the most popular ones as electrospinning or nano-imprint lithography, cannot fulfil all requirements in terms of alignment [26] [27], material constraints [28] [29], length [30], uniformity [31] [32], speed and cost [33] [34], yield and diversity [35]. In this work we report iterative thermal size reduction (ISR) technique, a novel fabrication method which is superior in all aspects considered above.

In Chapter 2 of this work, theoretical background of light scattering from nano-wires and nano-spheres is studied together with the comparison of different production methods for nano-wires as electrospinning, nano-imprint lithography and ISR. In Chapter 3, production and characterization of nano-wires and nano-spheres by ISR is widely explained and results are presented. In Chapter 4, structural coloration is introduced, theory of scattering from small particles is connected to structural coloration by estimation of scattering efficiency of nano-wires and nano-spheres for visible spectrum of light. Scattering efficiency is also simulated by using finite difference time domain (FDTD) method and results are compared with theoretical results. Observation of structural coloration in nano-wires and nano-spheres produced by ISR is presented. In the last chapter, Chapter 5, summary of work and future studies are discussed.

Chapter 2

Review

The theory of coloration of absorbtion and scattering from small particles is first developed in 1908 by Gustav Mie and later named as Mie theory [36]. In this study, Mie theory is recalled for small particles in several geometries as sphere, core-shell sphere, wire and core-shell wire starting from solution of wave equation to the estimation of scattering efficiency. In this chapter, derivation of electric and magnetic fields (E,H) task is done and in chapter 4 theory is connected to structural coloration by estimation of scattering efficiency using computer program based on the theory. Scattering for core-shell sphere and wire cases are simulated and results are compared with the theoretical results.

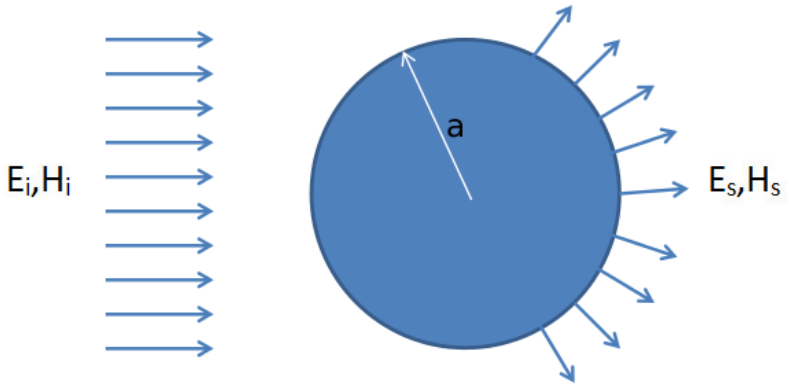

Figure 2.1: Scattering from nano-sphere.

2.1 Scattering From Small Particles: Mie Theory

2.1.1 Scattering by Nanospheres

2.1.1.1 Solutions to the vector wave equation

Time harmonic electromagnetic field (E,H fields) in a linear, isotropic and homogeneous medium (Figure 2.1) must satisfy the wave equations

$$\nabla^2 E + k^2 E = 0 \qquad \nabla^2 H + k^2 H = 0 \tag{2.1}$$

where $k^2 = \omega^2 \epsilon \mu$ and divergence of fields must be zero

$$\nabla \cdot E = 0 \qquad \nabla \cdot H = 0 \tag{2.2}$$

Furthermore, E and H fields are related to each other

$$\nabla \times E = iw\mu H \qquad \nabla \times H = -iw\epsilon E \tag{2.3}$$

At this point, vector field M is constructed by given scalar function ψ and constant vector c

$$M = \nabla \times (c\psi) \tag{2.4}$$

Since the divergence of the curl of any function vanishes

$$\nabla \cdot M = 0 \tag{2.5}$$

Using the vector identities:

$$\nabla \times (A \times B) = A(\nabla \cdot B) - B(\nabla \cdot A) + (B \cdot \nabla)A - (A \cdot \nabla)B \tag{2.6}$$

$$\nabla(A \cdot B) = A \times (\nabla \times B) + B \times (\nabla \times A) + (B \cdot \nabla)A + (A \cdot \nabla)B \tag{2.7}$$

we have

$$\nabla^2 M + k^2 M = \nabla \times [c(\nabla^2 \psi + k^2 \psi)] \tag{2.8}$$

So it means that if ψ is a solution of the scalar wave equation then M satisfies the vector wave equation.

$$\nabla^2 \psi + k^2 \psi = 0 \tag{2.9}$$

Let us also define N as a vector function as

$$N = \frac{\nabla \times M}{k} \tag{2.10}$$

N is also satisfies the vector wave equation with zero divergence.

$$\nabla \cdot N = 0 \tag{2.11}$$

$$\nabla^2 N + k^2 N = 0 \tag{2.12}$$

We also have

$$\nabla \times N = kM \tag{2.13}$$

Considering M and N are divergence-free, curl of one is proportional to other one and both satisfy the vector wave equation, they have all necessary properties of electromagnetic fields. Therefore our problem of having solutions to field equations become having solutions to scalar wave equation which is a simpler problem.

Thus, ψ is called the generating function for the vector harmonics (M, N), and c is called guiding vector. Since we have spherical symmetry, we choose our generating function in spherical coordinates and for the guiding vector we choose the radius r to obtain M as a solution of vector wave equation in spherical coordinates.

$$M = \nabla \times (r\psi) \tag{2.14}$$

The scalar wave equation in spherical coordinates is

$$\frac{1}{r^2}\frac{\partial}{\partial r}\left(r^2\frac{\partial \psi}{\partial r}\right) + \frac{1}{r^2 sin\theta}\frac{\partial}{\partial \theta}\left(sin\theta\frac{\partial \psi}{\partial \theta}\right) + \frac{1}{r^2 sin\theta}\frac{\partial^2 \psi}{\partial^2 \phi^2} + k^2\psi = 0 \tag{2.15}$$

With the separation of variables

$$\psi(r,\theta,\phi) = R(r)\Theta(\theta)\Phi(\phi) \tag{2.16}$$

We have

$$\frac{\partial^2\Phi}{\partial^2\phi} + m^2\phi = 0 \tag{2.17}$$

$$\frac{1}{sin\theta}\frac{d}{d\theta}\left(sin\theta\frac{d\Theta}{d\theta}\right) + \left[n(n+1) - \frac{m^2}{sin^2\theta}\right]\Theta = 0 \tag{2.18}$$

$$\frac{d}{dr}\left(r^2\frac{dR}{dr}\right) + [k^2r^2 - n(n+1)]R = 0 \tag{2.19}$$

constants m and n are determined due to the boundary conditions. For a given m, the linearly independent solutions to Equation 2.17 are

$$\Phi_e = cosm\phi \qquad\qquad \Phi_o = sinm\phi \tag{2.20}$$

where e and o denote even and odd solutions. Since ψ is a single valued function of ϕ

$$\lim_{\nu\to 2\pi}\psi(\phi+\nu) = \psi(\phi) \tag{2.21}$$

we need m to be zero or an integer. $(m = 0, 1, 2\cdots)$

The solution of Equation 2.18 is the associated Legendre functions of the first kind of degree n and order m, $P_n^m(cos\theta)$, where $n = m, m+1, \cdots$ and the orthogonality relations for these functions:

$$\int_{-1}^{1} P_n^m(\mu)P_{n'}^m(\mu)\,d\mu = \delta_{n'n}\frac{2}{2n+1}\frac{(n+m)!}{(n-m)!} \tag{2.22}$$

where $\mu = cos\theta$.

Let us define a dimensionless variable as $\rho = kr$ and a function $Z = R\sqrt{\rho}$,so Equation 2.19 becomes

$$\rho\frac{d}{d\rho}\left(\rho\frac{dZ}{d\rho}\right) + \left[\rho^2 - (n+\frac{1}{2})^2\right]Z = 0 \tag{2.23}$$

The linearly independent solutions of the Equation 2.23 are the Bessel functions of the first kind J_ν and the second kind Y_ν where $\nu = n+\frac{1}{2}$. So, the solutions of the Equation 2.19 are the spherical Bessel functions

$$j_n(\rho) = \sqrt{\frac{\pi}{2\rho}}J_{n+\frac{1}{2}}(\rho) \tag{2.24}$$

$$y_n(\rho) = \sqrt{\frac{\pi}{2\rho}}Y_{n+\frac{1}{2}}(\rho) \tag{2.25}$$

The recurrence relations of Bessel functions are

$$z_{n-1}(\rho) + z_{n+1}(\rho) = \frac{2n+1}{\rho}z_n(\rho) \tag{2.26}$$

$$(2n+1)\frac{d}{d\rho}z_n(\rho) = nz_{n-1}(\rho) - (n+1)z_{n+1}(\rho) \tag{2.27}$$

where z_n is either j_n or y_n. The first two orders are

$$j_0(\rho) = \frac{sin\rho}{\rho} \qquad j_1(\rho) = \frac{sin\rho}{\rho^2} - \frac{cos\rho}{\rho} \tag{2.28}$$

$$y_0(\rho) = -\frac{cos\rho}{\rho} \qquad y_1(\rho) = -\frac{cos\rho}{\rho^2} - \frac{sin\rho}{\rho} \tag{2.29}$$

and the higher orders can be obtained by recurrence relations.

Any two linear combination of j_n and y_n is also a more general solution and two of such combinations are spacial, the Bessel functions of the third kind i.e. the spherical Hankel functions,

$$h_n^{(1)}(\rho) = j_n(\rho) + iy_n(\rho) \tag{2.30}$$

$$h_n^{(2)}(\rho) = j_n(\rho) - iy_n(\rho) \tag{2.31}$$

After introducing the needed functions, let us construct our generating functions that satisfy the scalar wave equations in spherical coordinates.

$$\psi_{emn} = cos(m\phi)P_n^m(cos\theta)z_n(kr) \tag{2.32}$$

$$\psi_{omn} = sin(m\phi)P_n^m(cos\theta)z_n(kr) \tag{2.33}$$

where z_n is one of the Bessel functions $(j_n, y_n h_n^{(1)}, h_n^{(2)})$. The corresponding vector spherical harmonics M and N are

$$M_{emn} = \nabla \times (r\psi_{emn}) \qquad\qquad M_{omn} = \nabla \times (r\psi_{omn}) \tag{2.34}$$

$$N_{emn} = \frac{\nabla \times M_{emn}}{k} \qquad\qquad N_{omn} = \frac{\nabla \times M_{omn}}{k} \tag{2.35}$$

which can be written in broad form as

$$M_{emn} = \frac{-m}{sin\theta}sin(m\phi)P_n^m(cos\theta)z_n(\rho)\hat{\theta} - cos(m\phi)\frac{dP_n^m(cos\theta)}{d\theta}z_n(\rho)\hat{\phi} \tag{2.36}$$

$$M_{omn} = \frac{m}{sin\theta}cos(m\phi)P_n^m(cos\theta)z_n(\rho)\hat{\theta} - sin(m\phi)\frac{dP_n^m(cos\theta)}{d\theta}z_n(\rho)\hat{\phi} \tag{2.37}$$

$$N_{emn} = \begin{cases} \frac{z_n(\rho)}{\rho} cos(m\phi) n(n+1) P_n^m(cos\theta)\hat{r} \\ \\ +cos(m\phi) \frac{dP_n^m(cos\theta)}{d\theta} \frac{1}{\rho} \frac{d}{d\rho}[\rho z_n(\rho)]\hat{\theta} \\ \\ -msin(m\phi) \frac{P_n^m(cos\theta)}{sin\theta} \frac{1}{\rho} \frac{d}{d\rho}[\rho z_n(\rho)]\hat{\phi} \end{cases} \tag{2.38}$$

$$N_{omn} = \begin{cases} \frac{z_n(\rho)}{\rho} sin(m\phi) n(n+1) P_n^m(cos\theta)\hat{r} \\ \\ +sin(m\phi) \frac{dP_n^m(cos\theta)}{d\theta} \frac{1}{\rho} \frac{d}{d\rho}[\rho z_n(\rho)]\hat{\theta} \\ \\ +mcos(m\phi) \frac{P_n^m(cos\theta)}{sin\theta} \frac{1}{\rho} \frac{d}{d\rho}[\rho z_n(\rho)]\hat{\phi} \end{cases} \tag{2.39}$$

2.1.1.2 Expansion of a plane wave in vector spherical harmonics

In our case we are concerned about scattering of a plane wave. The x polarized plane wave in spherical coordinates is denoted by

$$E_i = E_0 e^{ikrcos\theta}\hat{x} \tag{2.40}$$

where

$$\hat{x} = sin\theta cos\phi\hat{r} + cos\theta cos\phi\hat{\theta} - sin\phi\hat{\phi} \tag{2.41}$$

In terms of vector spherical coordinates we expand Equation 2.40

$$E_i = \sum_{m=0}^{\infty}\sum_{n=0}^{\infty}(B_{emn}M_{emn} + B_{omn}M_{omn} + A_{emn}N_{emn} + A_{omn}N_{omn}) \tag{2.42}$$

since $sinm\phi$ is orthogonal to $cosm'\phi$ we have M_{emn} is orthogonal to M_{omn}

$$\int_0^{2\pi}\int_0^{\pi} M_{em'n'} \cdot M_{omn} sin\theta \, d\theta \, d\phi = 0 \tag{2.43}$$

and similarly (N_{emn}, N_{omn}) (M_{omn}, N_{omn}) and (M_{emn}, N_{emn}) are orthogonal sets. Also any two vector harmonics with different m are orthogonal to each other.

In the case of (M_{emn}, N_{omn}) and (M_{omn}, N_{emn}) to prove orthogonality we have

$$m\int_o^{\pi}\left(P_n^m \frac{dP_{n'}^m}{d\theta} + P_{n'}^m \frac{dP_n^m}{d\theta}\right) d\theta = P_n^m P_{n'}^m|_0^{\pi} \tag{2.44}$$

Here the associated Legendre function P_n^m is related to P_n as

$$P_n^m(\mu) = (1-\mu^2)^{\frac{m}{2}} \frac{d^m P_n(\mu)}{d\mu^m} \tag{2.45}$$

where $\mu = cos\theta$. Since P_n^m is related to m'th derivative of P_n, P_n^m vanishes for $\theta = 0, \pi$ except $m = 0$ case. Therefore, Equation 2.44 vanishes for all m, n and n'.

The orthogonality for the remaining cases

$$\int_0^{2\pi}\int_0^{\pi} M_{emn} \cdot M_{emn'} sin\theta \, d\theta \, d\phi = \int_0^{2\pi}\int_0^{\pi} M_{omn} \cdot M_{omn'} sin\theta \, d\theta \, d\phi = 0 \tag{2.46}$$

$$\int_0^{2\pi}\int_0^{\pi} N_{emn} \cdot N_{emn'} sin\theta \, d\theta \, d\phi = \int_0^{2\pi}\int_0^{\pi} N_{omn} \cdot N_{omn'} sin\theta \, d\theta \, d\phi = 0 \tag{2.47}$$

where $n \neq n'$ and $m \neq 0$. It is required to show that

$$\int_0^{\pi}\left(\frac{dP_n^m}{d\theta}\frac{dP_{n'}^m}{d\theta} + m^2 \frac{P_n^m P_{n'}^m}{sin^2\theta}\right) sin\theta \, d\theta = 0 \tag{2.48}$$

since P_n^m and $P_{n'}^m$ both satisfy Equation 2.18, after some mathematical manipulation we have

$$2sin\theta\left(\frac{dP_n^m}{d\theta}\frac{dP_{n'}^m}{d\theta}+m^2\frac{P_n^m P_{n'}^m}{sin^2\theta}\right)=\begin{cases}[n(n+1)+n'(n'+1)]P_n^m P_{n'}^m sin\theta \\ \\ +\frac{d}{d\theta}\left(sin\theta\frac{dP_{n'}^m}{d\theta}P_n^m+sin\theta\frac{dP_n^m}{d\theta}P_{n'}^m\right)\end{cases} \tag{2.49}$$

and together with the orthogonality relations for P_n^m, Equation 2.48 is proved.

Based on these orthogonality relations, the coefficients in the expansion Equation 2.42 are of the form:

$$B_{emn}=\frac{\int_0^{2\pi}\int_0^{\pi}E_i\cdot M_{emn}sin\theta\,d\theta\,d\phi}{\int_0^{2\pi}\int_0^{\pi}|M_{emn}|^2 sin\theta\,d\theta\,d\phi} \tag{2.50}$$

and similarly for B_{omn}, A_{emn} and A_{omn}. With the orthogonality of sin and cos, Equations 2.36, 2.39 and 2.41 follows that $B_{emn}=A_{omn}=0$ for all m and n and the other coefficient vanishes except $m=1$. Since the incident field is finite at the origin, we reject y_n. We will use superscript (1) for the vector harmonics to show them radial dependance of generating function is specified by j_n. So, the incident field has the form:

$$E_i=\sum_{n=1}^{\infty}(B_{oln}M_{oln}^{(1)}+A_{eln}N_{eln}^{(1)}) \tag{2.51}$$

Using Equation 2.36 one can evaluate the integral at the denominator in the expression for B_{oln}. However we have the integral at the nominator:

$$\int_0^{\pi}\frac{d}{d\theta}(sin\theta P_n^l)e^{i\rho cos\theta}\,d\theta \tag{2.52}$$

from Equation 2.45,

$$P_n^l=\frac{-dP_n}{d\theta} \tag{2.53}$$

where Legendre polynomials of degree n satisfy the Equation 2.18

$$\frac{d}{d\theta}\left(sin\theta\frac{dP_n}{d\theta}\right) = -n(n+1)P_n sin\theta \tag{2.54}$$

So, Equation 2.52 is proportional to

$$\int_0^\pi e^{i\rho cos\theta} P_n sin\theta \, d\theta \tag{2.55}$$

For the last step we will use Genenbauer's generalization for the Poisson's integral.

$$j_n(\rho) = \frac{i^{-n}}{2}\int_0^\pi e^{i\rho cos\theta} P_n sin\theta \, d\theta \tag{2.56}$$

So for the B_{oln}

$$B_{oln} = i^n E_0 \frac{2n+1}{n(n+1)} \tag{2.57}$$

For the A_{emn} our task is easier. When we are faced with the integral

$$\int_0^\pi P_n^l sin\theta e^{i\rho cos\theta} sin\theta \, d\theta \tag{2.58}$$

using the Equations 2.53, 2.54 and 2.56 and integration by parts we have the solution:

$$\frac{2n(2n+1)j_n(\rho)i^n}{i\rho} \tag{2.59}$$

For the case of the integral

$$\int_0^\pi \left(cos\theta\frac{dP_n^l}{d\theta} + \frac{P_n^l}{sin\theta}\right) e^{i\rho cos\theta} sin\theta \, d\theta \tag{2.60}$$

which is result of first multiplying Equation 2.56 by ρ and differentiating it with respect to ρ. After a bit of algebra we have

$$\frac{2n(2n+1)i^n}{i\rho}\frac{d}{d\rho}(\rho j_n) \tag{2.61}$$

Then A_{eln} follows

$$A_{eln} = iE_0 i^n \frac{2n+1}{n(n+1)} \tag{2.62}$$

and the incident field E_i becomes

$$E_i = E_0 \sum_{n=1}^{\infty} i^n \frac{2n+1}{n(n+1)}(M_{oln}^{(1)} - iN_{eln}^{(1)}) \tag{2.63}$$

2.1.1.3 Internal and scattered fields

Suppose we have incident x-polarized plane wave as denoted in the Equation 2.63. Corresponding H field is obtained by curl of E field as

$$H_i = \frac{-k}{\omega\mu}E_0 \sum_{n=1}^{\infty} i^n \frac{2n+1}{n(n+1)}(M_{eln}^{(1)} + iN_{oln}^{(1)}) \tag{2.64}$$

For the scattered fields (E_s, H_s) and the internal fields (E_1, H_1) we have the boundary conditions

$$(E_i + E_s - E_1) \times \hat{r} = (H_i + H_s - H_1) \times \hat{r} = 0 \tag{2.65}$$

Solving for inside fields (E_1, H_1), due to the same reasons above, all the coefficients of vector harmonics vanishes except $m = 1$ and we take $j_n(k_1 r)$ where k_1 is the wave number in sphere.

$$E_1 = \sum_{n=1}^{\infty} E_n(c_n M_{oln}^{(1)} - id_n N_{eln}^{(1)}) \tag{2.66}$$

$$H_1 = \frac{-k}{\omega\mu_1} \sum_{n=1}^{\infty} E_n(d_n M_{eln}^{(1)} + ic_n N_{oln}^{(1)}) \tag{2.67}$$

where $E_n = i^n E_0(2n+1)/(n(n+1))$ and permeability of sphere denoted by μ_1.

In the outside region, y_n is also valid as j_n so, in the solution we use Hankel functions h_n^1 and h_n^2 of order ν

$$H_\nu^{(1)}(\rho) \sim \sqrt{\frac{2}{\pi\rho}} e^{i[\rho - \frac{\nu\pi}{2} - \frac{\pi}{4}]} \sum_{m=0}^{\infty} \frac{(-1)^m(\nu, m)}{(2i\rho)^m} \tag{2.68}$$

$$H_\nu^{(2)}(\rho) \sim \sqrt{\frac{2}{\pi\rho}} e^{-i[\rho - \frac{\nu\pi}{2} - \frac{\pi}{4}]} \sum_{m=0}^{\infty} \frac{(\nu, m)}{(2i\rho)^m} \tag{2.69}$$

where $(\nu, m) = \Gamma(\nu + m + 1/2)/(m!\Gamma(\nu - m + 1/2))$ and Γ is the Gamma function. So, asymptotically, Equations 2.68 and 2.69 behave as

$$h_n^{(1)}(kr) \sim \frac{(-i)^n e^{ikr}}{ikr} \qquad kr >> n^2 \tag{2.70}$$

$$h_n^{(2)}(kr) \sim -\frac{i^n e^{-ikr}}{ikr} \qquad kr >> n^2 \tag{2.71}$$

Here $h_n^{(1)}$ corresponds to an outgoing wave while h_n^2 corresponds to an incoming wave. Therefore, for the asymptotic case we just need to have outgoing wave in the region outside of the sphere so h_n^2 term should be neglected.

For the asymptotic case, an expression of the derivatives of h_n^1 is required. It follows from

$$\frac{d}{d\rho}z_n = \frac{nz_{n-1} - (n+1)z_{n+1}}{2n+1} \tag{2.72}$$

and together with the Equation 2.70 we have

$$\frac{dh_n^{(1)}}{d\rho} \sim \frac{(-i)^n e^{i\rho}}{\rho} \qquad (\rho >> n^2) \tag{2.73}$$

The scattered fields are therefore:

$$E_s = \sum_{n=1}^{\infty} E_n(ia_n N_{eln}^{(3)} - b_n M_{oln}^{(3)}) \tag{2.74}$$

$$H_s = \frac{k}{\omega\mu} \sum_{n=1}^{\infty} E_n(ib_n N_{oln}^{(3)} + a_n M_{eln}^{(3)}) \tag{2.75}$$

Where we use the superscript (3) to show the radial dependance of the generating function is specified by h_n^1.

2.1.2 Scattering by Core-Shell Nano-Spheres

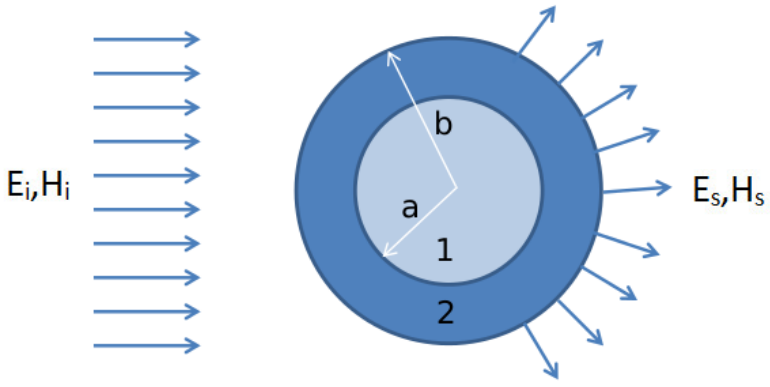

Figure 2.2: Scattering from core-shell nano-sphere.

In this section we develop mathematical formulations for scattering from core-shell nano-sphere (Figure 2.2) which has inner radius a and outher radius b. Suppose we have incident electromagnetic field as described in Equations 2.63 and 2.64. Resulting electromagnetic field for the region $r < a$, (E_1, H_1), is given in Equations 2.66 and 2.67 and for the region $r > b$, (E_s, H_s), is given in Equations 2.74 and 2.75. Electromagnetic field for the only remaining region $b < r < a$, (E_2, H_2) is must be expanded as

$$E_2 = \sum_{n=1}^{\infty} E_n(f_n M_{oln}^{(1)} - ig_n N_{eln}^{(1)} + v_n M_{oln}^{(2)} - iw_n N_{eln}^{(2)}) \tag{2.76}$$

$$H_2 = -\frac{k_2}{w\mu_2} \sum_{n=1}^{\infty} E_n[g_n M_{eln}^{(1)} + if_n N_{oln}^{(1)} + w_n M_{eln}^{(2)} + iv_n N_{oln}^{(2)}] \tag{2.77}$$

where the vector harmonics denoted by superscript (2) are generated by functions of the form denoted in the Equations 2.32 and 2.33 with redial dependance $y_n(k_2 r)$, since j_n and y_n are both finite in this region. The boundary conditions

$$(E_2 - E_1) \times \hat{r} = 0 \qquad (H_2 - H_1) \times \hat{r} = 0 \qquad where \qquad r = a \tag{2.78}$$

$$(E_s + E_i - E_2) \times \hat{r} = 0 \qquad (H_s + H_i - H_2) \times \hat{r} = 0 \qquad where \qquad r = b \tag{2.79}$$

yield the eight equation with coefficients $a_n\ b_n\ c_n\ d_n\ f_n\ g_n\ v_n\ w_n$.

$$f_n m_1 \psi_n(m_2 x) - v_n m_1 X_n(m_2 x) - c_n m_2 \psi_n(m_1 x) = 0 \tag{2.80}$$

$$w_n m_1 X_n'(m_2 x) - g_n m_1 \psi_n'(m_2 x) - d_n m_2 \psi_n'(m_1 x) = 0 \tag{2.81}$$

$$v_n \mu_1 X_n'(m_2 x) - f_n \mu_1 \psi_n'(m_2 x) - c_n \mu_2 \psi_n'(m_1 x) = 0 \tag{2.82}$$

$$g_n\mu_1\psi_n(m_2x) - w_n\mu_1 X_n(m_2x) - d_n\mu_2\psi_n(m_1x) = 0 \tag{2.83}$$

$$m_2\psi_n'(y) - a_n m_2\xi_n'(y) - g_n\psi_n'(m_2y) + w_n X_n'(m_2y) = 0 \tag{2.84}$$

$$m_2 b_n\xi_n(y) - m_2\psi_n(y) f_n\psi_n(m_2y) - v_n X_n(m_2y) = 0 \tag{2.85}$$

$$\mu_2\psi_n(y) - a_n\mu_2\xi_n(y) - g_n\mu\psi_n(m_2y) + w_n\mu X_n(m_2y) = 0 \tag{2.86}$$

$$b_n\mu_2\xi_n'(y) - \mu_2\psi_n'(y) + f_n\mu\psi_n'(m_2y) - v_n\mu X_n'(m_2y) = 0 \tag{2.87}$$

where m_1 and m_2 are refractive indices of core and coating part respectively relative to surrounding medium, μ, μ_1 and μ_2 are permeabilities of the surrounding medium, core and coating part respectively. $x = ka$ and $y = kb$. The Riccati-Bessel function $X_n(z) = -zy_n(z)$.

2.1.3 Scattering by Core-Shell Nano-Wires

Again we start with the same arguments as we did for the spherical case from the scalar wave equation $\nabla^2\psi + k^2\psi = 0$ but this time we consider cylindrical coordinates

$$\frac{1}{r}\frac{\partial}{\partial r}\left(r\frac{\partial\psi}{\partial r}\right) + \frac{1}{r^2}\frac{\partial^2\psi}{\partial\phi^2} + \frac{\partial^2\psi}{\partial z^2} + k^2\psi = 0 \tag{2.88}$$

With the separation of variables we have

$$\psi_n(r,\phi,z) = Z_n(\rho)e^{in\phi}e^{ihz} \qquad (n = 0, \pm1, \cdots) \tag{2.89}$$

where $\rho = r\sqrt{k^2 - h^2}$ and Z_n is the solution for the Bessel equation

$$\rho \frac{d}{d\rho}\left(\rho \frac{d}{d\rho} Z_n\right) + (\rho^2 - n^2) Z_n = 0 \tag{2.90}$$

Linearly independent solutions to the Equation 2.90 are Bessel functions of the first, J_n and second kind, Y_n. Vector cylindrical harmonics generated from the Equation 2.89 are:

$$M_n = \nabla \times (\hat{z}\psi_n) \qquad\qquad N_n = \frac{\nabla \times M_n}{k} \tag{2.91}$$

where the pilot vector taken as $\hat{z}$ which is parallel to cylinder axis. In broader form vector harmonics are:

$$M_n = \sqrt{k^2 - h^2}\left(in\frac{Z_n(\rho)}{\rho}\hat{r} - Z_n'(\rho)\hat{\phi}\right) e^{i(n\phi + hz)} \tag{2.92}$$

$$N_n = \frac{\sqrt{k^2 - h^2}}{k}\left(ihZ_n'(\rho)\hat{r} - hn\frac{Z_n(\rho)}{\rho}\hat{\phi} + \sqrt{k^2 - h^2}Z_n(\rho)\hat{z}\right) e^{i(n\phi + hz)} \tag{2.93}$$

The orthogonality of vector harmonics follows

$$\int_0^{2\pi} M_n \cdot M_n^* \, d\phi = \int_0^{2\pi} N_n \cdot N_m^* \, d\phi = \int_0^{2\pi} M_n \cdot N_m^* \, d\phi = 0 \tag{2.94}$$

Let us consider an infinite core-shell wire with inner radius a and outer radius b which is illuminated by a incident plane wave denoted as $E_i = E_0 e^{ik\hat{i}\cdot x}$ and the propagation direction $\hat{i} = -sin\zeta\hat{x} - cos\zeta\hat{z}$ where ζ is the angle between cylinder axis and the incident wave. In this case we have two possible orthogonal polarization state. Electric field is polarized parallel or perpendicular to the xz plane.

Case1: E_i is parallel to the xz plane (TM case)

We expend E

$$E_i = E_0(sin\zeta\hat{z} - cos\zeta\hat{x})e^{-ik(rsin\zeta cos\phi + zcos\zeta)} \tag{2.95}$$

in terms of vector cylindrical harmonics but to have finite solution at $r = 0$ we need to exclude Y_n from the radial part of the solution. Also it is clear that the h from the Equation 2.89 must be $-kcos\zeta$. Thus

$$E_i = \sum_{n=-\infty}^{\infty} \left[A_n M_n^{(1)} + B_n N_n^{(1)}\right] \tag{2.96}$$

where the vector harmonics are generated from $J_n(krsin\zeta)e^{in\phi}e^{-ikzcos\zeta}$ and to find coefficients A_n and B_n we need to use orthogonality of vector harmonics in which we need to evaluate the integral equations:

$$I_n^{(1)} = \int_0^{2\pi} e^{-i(n\phi + \rho cos\phi)\, d\phi} \tag{2.97}$$

$$I_n^{(2)} = \int_0^{2\pi} e^{-i(n\phi + \rho cos\phi)cos\phi\, d\phi} \tag{2.98}$$

$$I_n^{(3)} = \int_0^{2\pi} e^{-i(n\phi + \rho cos\phi)sin\phi\, d\phi} \tag{2.99}$$

where $\rho = krsin\zeta$. From the representation of $J_n(\rho)$ in the integral form

$$J_n(\rho) = \frac{i^{-n}}{2\pi} \int_0^{2\pi} e^{i(n\phi + \rho cos\phi)\, d\phi} \tag{2.100}$$

it follows that $I_n^{(1)} = 2\pi(-i)^n J_n(\rho)$ and differentiating it we obtain $I_n^{(2)} = 2\pi i(-i)^n J_n'(\rho)$. We obtain third integral by

$$2iI_n^{(3)} = I_{n-1}^{(1)} - I_{n+1}^{(1)} \tag{2.101}$$

and using the identity

$$\frac{2nZ_n}{\rho} = Z_{n-1} + Z_{n+1} \tag{2.102}$$

we have $I_n^{(3)} = 2\pi(-i)^n J_n(\rho)n/\rho$ and using these integrals we have

$$A_n = 0 \qquad\qquad B_n = \frac{E_0(-i)^n}{ksin\zeta} \tag{2.103}$$

Therefore the expansion of E_i follows as

$$E_i = \sum_{n=-\infty}^{\infty} E_n N_n^{(1)} \qquad\qquad H_i = \frac{-ik}{\omega\mu} \sum_{n=-\infty}^{\infty} E_n M_n^{(1)} \tag{2.104}$$

where $E_n = E_0(-i)^n/ksin\zeta$.

The boundary conditions are:

$$(E_2 - E_1) \times \hat{r} = 0 \qquad (H_2 - H_1) \times \hat{r} = 0 \qquad where \qquad r = a \tag{2.105}$$

$$(E_s + E_i - E_2) \times \hat{r} = 0 \qquad (H_s + H_i - H_2) \times \hat{r} = 0 \qquad where \qquad r = b \tag{2.106}$$

To satisfy continuity at the boundaries, the separation constant h in the wave equation must also be $-kcos\zeta$. Finiteness at $r = 0$ requires to use J_n as the appropriate Bessel function and the generating functions for the core field, (E_1, H_1) are $J_n(kr\sqrt{m^2 - cos^2\zeta})e^{in\phi}e^{-ikzcos\zeta}$ where m is the relative refractive index of the core. Corresponding expansions are:

$$E_1 = \sum_{n=-\infty}^{\infty} E_n \left[g_n M_n^{(1)} + f_n N_n^{(1)} \right] \tag{2.107}$$

$$H_1 = \frac{-ik_1}{\omega\mu_1} \sum_{n=-\infty}^{\infty} E_n \left[g_n N_n^{(1)} + f_n M_n^{(1)} \right] \tag{2.108}$$

and for the shell field, (E_2, H_2), we also use Y_n which is also finite in the shell region

$$E_2 = \sum_{n=-\infty}^{\infty} E_n \left(g_n M_n^{(2j)} + f_n N_n^{(2j)} + v_n M_n^{(2y)} + w_n N_n^{(2y)} \right) \tag{2.109}$$

$$H_2 = \frac{-ik}{\omega\mu} \sum_{n=-\infty}^{\infty} E_n \left(f_n M_n^{(2j)} + g_n N_n^{(2j)} + w_n M_n^{(2y)} + v_n N_n^{(2y)} \right) \tag{2.110}$$

For the Equation 2.90, the Hankel functions, $H_n^{(1)} = J_n + iY_n$ and $H_n^{(2)} = J_n - iY_n$ are also the linearly independent solutions which are asymptotically:

$$H_n^{(1)}(\rho) \sim \sqrt{\frac{2}{\pi\rho}} e^{i\rho}(-i)^n e^{-i\pi/4} \qquad |\rho| >> n^2 \tag{2.111}$$

$$H_n^{(2)}(\rho) \sim \sqrt{\frac{2}{\pi\rho}} e^{i\rho} i^n e^{i\pi/4} \qquad |\rho| >> n^2 \tag{2.112}$$

Therefore the outgoing scattering wave, (E_s, H_s):

$$E_s = -\sum_{n=-\infty}^{\infty} E_n \left[b_{n1} N_n^{(3)} + i a_{n1} M_n^{(3)} \right] \tag{2.113}$$

$$H_s = \frac{ik}{\omega\mu} \sum_{n=-\infty}^{\infty} E_n \left[b_{n1} M_n^{(3)} + i a_{n1} N_n^{(3)} \right] \tag{2.114}$$

must be $H_n^{(1)}(krsin\zeta)e^{in\phi}e^{-ikzcos\zeta}$.

Case2: E_i is perpendicular to the xz plane (TE case)

In this case, $E_i = E_0\hat{y}e^{-ik(rsin\zeta cos\phi + zcos\zeta)}$ and the expansion of incident field is:

$$E_i = -i \sum_{n=-\infty}^{\infty} E_n M_n^{(1)} \tag{2.115}$$

The curl of it gives the magnetic field

$$H_i = \frac{-k}{\omega\mu} \sum_{n=-\infty}^{\infty} E_n N_n^{(1)} \tag{2.116}$$

and after the same process we had for case1, the fields are:

$$E_1 = -i \sum_{n=-\infty}^{\infty} E_n \left(c_n M_n^{(1)} + d_n N_n^{(1)} \right) \tag{2.117}$$

$$H_1 = \frac{-k_1}{\omega\mu_1} \sum_{n=-\infty}^{\infty} E_n \left(c_n N_n^{(1)} + d_n M_n^{(1)} \right) \tag{2.118}$$

$$E_2 = -i \sum_{n=-\infty}^{\infty} E_n \left(g_n M_n^{(2j)} + f_n N_n^{(2j)} + v_n M_n^{(2y)} + w_n N_n^{(2y)} \right) \tag{2.119}$$

$$H_2 = \frac{-k_2}{\omega\mu_2} \sum_{n=-\infty}^{\infty} E_n \left(f_n M_n^{(2j)} + g_n N_n^{(2j)} + w_n M_n^{(2y)} + v_n N_n^{(2y)} \right) \tag{2.120}$$

$$E_s = \sum_{n=-\infty}^{\infty} E_n \left(b_{n2} N_n^{(3)} + i a_{n2} M_n^{(3)} \right) \tag{2.121}$$

$$H_s = \frac{k}{\omega\mu} \sum_{n=-\infty}^{\infty} E_n \left(i b_{n2} M_n^{(3)} + a_{n2} N_n^{(3)} \right) \tag{2.122}$$

Here is the bare forms of M and N wave-vectors of all three regions for the core-shell nano-wire.

$$M_n^i = ksin\gamma \left(in \frac{J_n(krsin\gamma)}{krsin\gamma} \hat{r} - J_n'(krsin\gamma)\hat{\phi} \right) e^{i(n\phi - kzcos\gamma)} \tag{2.123}$$

$$N_n^i = \begin{pmatrix} sin\gamma - ikcos\gamma J_n'(krsin\gamma)\hat{r} \\ \\ +kncos\gamma \frac{J_n(krsin\gamma)}{krsin\gamma}\hat{\phi} \\ \\ +ksin\gamma J_n(krsin\gamma)\hat{z} \end{pmatrix} e^{i(n\phi - kzcos\gamma)} \tag{2.124}$$

$$M_n^3 = ksin\gamma \left(in\frac{H_n^1(krsin\gamma)}{krsin\gamma}\hat{r} - H_n'^1(krsin\gamma)\hat{\phi} \right) e^{i(n\phi - kzcos\gamma)} \tag{2.125}$$

$$N_n^3 = \begin{pmatrix} sin\gamma - ikcos\gamma H_n'^1(krsin\gamma)\hat{r} \\ \\ +kncos\gamma \frac{H_n^1(krsin\gamma)}{krsin\gamma}\hat{\phi} \\ \\ +ksin\gamma H_n^1(krsin\gamma)\hat{z} \end{pmatrix} e^{i(n\phi - kzcos\gamma)} \tag{2.126}$$

$$M_n^1 = k_1 sin\gamma \left(in\frac{J_n(kr\sqrt{m_1^2 - cos^2\gamma})}{k_1 rsin\gamma}\hat{r} - J_n'(kr\sqrt{m_1^2 - cos^2\gamma})\hat{\phi} \right) e^{i(n\phi - kzcos\gamma)} \tag{2.127}$$

$$N_n^1 = \begin{pmatrix} sin\gamma - ikcos\gamma J_n'(kr\sqrt{m_1^2 - cos^2\gamma})\hat{r} \\ \\ +k_1 ncos\gamma \frac{J_n(kr\sqrt{m_1^2 - cos^2\gamma})}{k_1 rsin\gamma}\hat{\phi} \\ \\ +k_1 sin\gamma J_n(kr\sqrt{m_1^2 - cos^2\gamma})\hat{z} \end{pmatrix} e^{i(n\phi - kzcos\gamma)} \tag{2.128}$$

$$M_n^{2j} = k_2 sin\gamma \left(in\frac{J_n(kr\sqrt{m_2^2 - cos^2\gamma})}{k_2 rsin\gamma}\hat{r} - J_n'(kr\sqrt{m_2^2 - cos^2\gamma})\hat{\phi} \right) e^{i(n\phi - kzcos\gamma)} \tag{2.129}$$

$$N_n^{2j} = \begin{pmatrix} sin\gamma - ik_2 cos\gamma J_n'(kr\sqrt{m_2^2 - cos^2\gamma})\hat{r} \\ \\ +k_2 n cos\gamma \frac{J_n(kr\sqrt{m_2^2-cos^2\gamma})}{k_2 r sin\gamma}\hat{\phi} \\ \\ +k_2 sin\gamma J_n(kr\sqrt{m_2^2 - cos^2\gamma})\hat{z} \end{pmatrix} e^{i(n\phi - kzcos\gamma)} \tag{2.130}$$

$$M_n^{2y} = k_2 sin\gamma \left(in\frac{Y_n(kr\sqrt{m_2^2 - cos^2\gamma})}{k_1 r sin\gamma}\hat{r} - Y_n'(kr\sqrt{m_2^2 - cos^2\gamma})\hat{\phi} \right) e^{i(n\phi - kzcos\gamma)} \tag{2.131}$$

$$N_n^{2y} = \begin{pmatrix} sin\gamma - ik_2 cos\gamma Y_n'(kr\sqrt{m_2^2 - cos^2\gamma})\hat{r} \\ \\ +k_2 n cos\gamma \frac{Y_n(kr\sqrt{m_2^2-cos^2\gamma})}{k_2 r sin\gamma}\hat{\phi} \\ \\ +k_2 sin\gamma Y_n(kr\sqrt{m_2^2 - cos^2\gamma})\hat{z} \end{pmatrix} e^{i(n\phi - kzcos\gamma)} \tag{2.132}$$

2.2 Fabrication Techniques for Producing Nano-Wires

Undeniably, nano-wires are one of the most practised nano-structured material types [33] [34]. Recent studies result remarkable growth in producing complex nano-wire structures [22] [23]. However, in terms of repeatability and device integration, serious development is required [37] [38] [39]. Here is the comparison of popular production methods for nano-wires as electrospinning and nano-imprint lithography versus our novel method ISR.

Electrospinning is a solvent dependent method which uses both electrospraying and dry spinning to create fibers with micro-sized or nano-sized diameters [40]. Process starts with applying high voltage to a liquid droplet. When droplet become charged, because of electronic repulsion, surface tension cannot keep droplet in sphere form and droplet stretches. At a certain point, liquid stream erupts from the droplet forming a cone called Taylor Cone. If the cohesion forces that keep liquid intact is strong enough, liquid stream does not break and charged liquid forms a jet. As the jet dries to form fiber, charges move to the surface of the fiber and fiber is elongated because of whipping process caused by electrostatic forces till it reaches to the grounded target. Elongation and thinning results nano-scale fibers [41] (Figure 2.3 and 2.4).

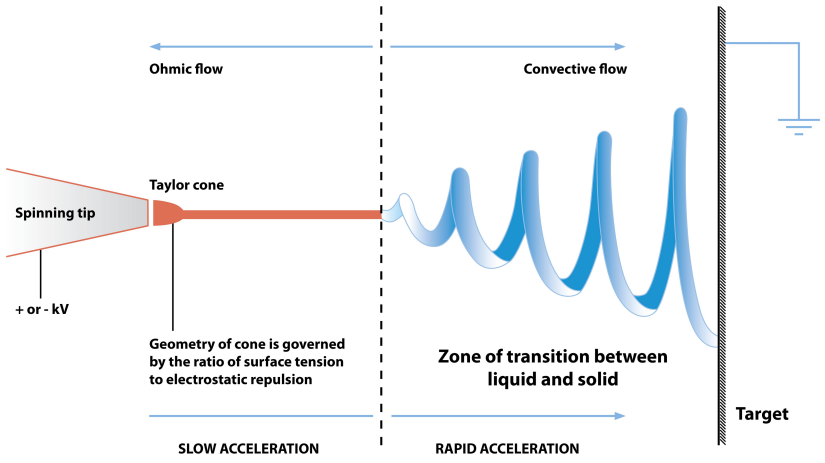

Figure 2.3: A diagram that shows fiber production by electrospinning.

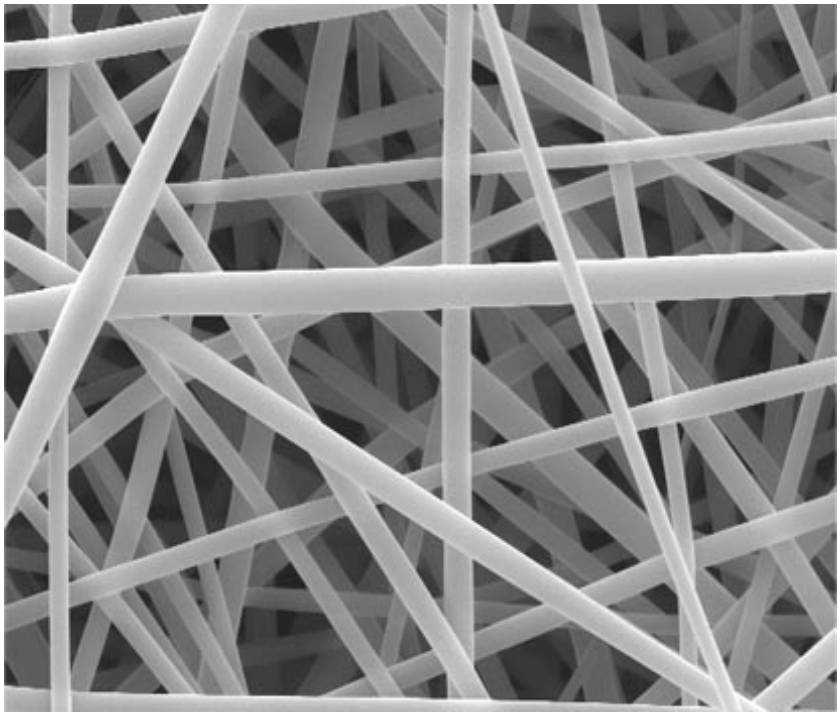

Figure 2.4: A SEM image that shows fibers produced by electrospinning [42].

Nano-imprint lithography is also a solvent dependent method which creates nano-scale patterns by mechanical deformation of the imprint resist. It has two basic steps. In first step, a mold with nano-structures that we want onto it is pressed into a thin resist layer which is on the substrate. After removal of the mold we have our structures on the resist layer. In the second step, an anisotropic etching method as RIE (Reactive Ion Etching) is used to remove resist layer in the compressed field. After this step pattern is transferred into the entire resist [43] [44] (Figure 2.5 and 2.6).

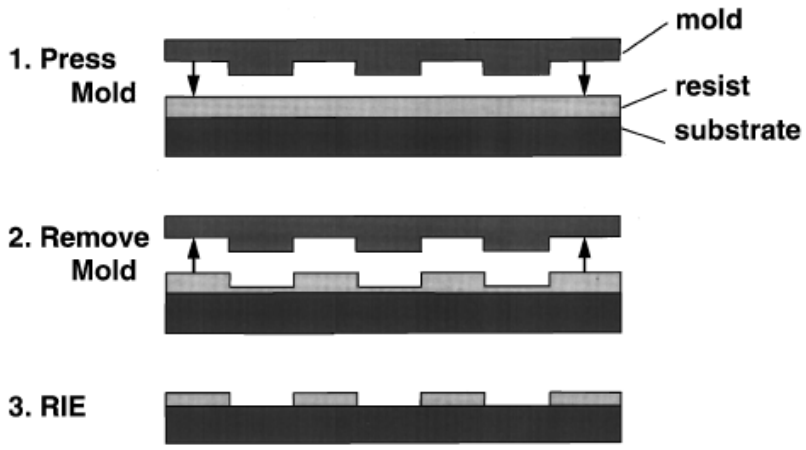

Figure 2.5: A schematic diagram shows nano-imprint lithography [43] (1) imprinting using a mold (2) removal of mold (3) pattern transfer using anisotropic etching to remove residue resist in the compressed areas.

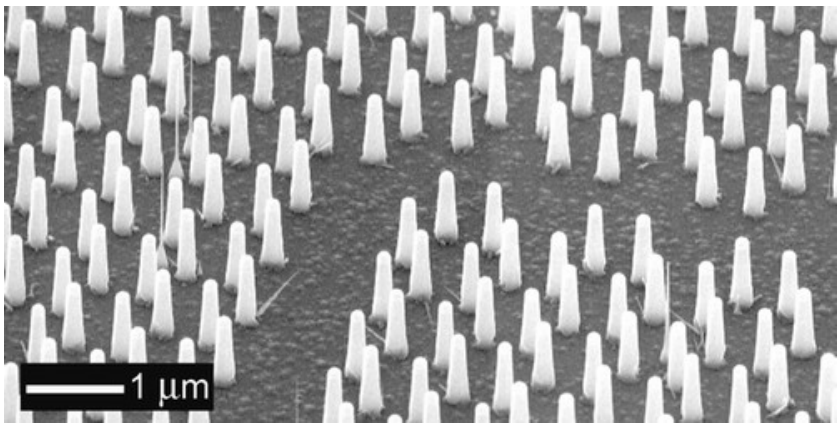

Figure 2.6: A SEM image that hows fibers produced by nano-imprint lithograpy [45].

Although these methods are appropriate to produce polymer fibers, when considering nano-wire aspect ratio, uniformity, size and geometry control, yield and device integrability, these methods are not superior (Table 2.1). Using electrospinning, nanowires with high aspect ratio and with high yield can be produced but in terms of uniformity and geometry control, electrospinning is not an appropriate method. Also by nano-imprint lithography, uniform nano-wires can be produced with tunable diameters but, in terms of multi-material compatibility and yield, nano-imprint lithography is also not an optimum technique. Unlike

these two methods, ISR method which is widely described in chapter 3, can be used to produce nano-wires with high aspect ratio, excellent uniformity, desired geometry and with high yield [46] [47] [48].

	Electrospinning	Lithography	ISR
Aspect Ratio	Excellent	Poor	Excellent
Uniformity	Poor	Excellent	Excellent
Size Control	Good	Excellent	Excellent
Geometry Control	Poor	Excellent	Excellent
Multi Material Compatibility	Poor	Poor	Excellent
Yield	Excellent	Poor	Excellent
Large Area Device Integrability	Poor	Good	Excellent

Table 2.1: Quality comparison of different production methods for nano-wires.

Chapter 3

Production and Characterization of Micro and Nano-Structures

3.1 Preparation of Macroscopic Preform

The macroscopic shape of the fiber before thermal drawing process is called preform. Preparation of preform is the most crucial step of fiber production process since a damage occurs in the preform will inevitably be observed throughout the fiber. A preform generally has cylinder shape with $2-3$ centimeters diameter and $15-35$ centimeter length (Figure 3.1). Materials used in preform must have nearly same glass transition temperatures since thermal size reduction process will be performed at this temperature (Figure 3.2).

Figure 3.1: A preform (a) before fiber drawing process (b) after fiber drawing process.

3.1.1 Preform Design

In this study, designed preform has three main parts, core, cladding and jacket. Jacket part consists of polymer. By arranging its diameter, jacket will let us reduce the diameter of preform as we want. Simply, for reduction factor of 100, to obtain fiber with 300 μm diameter we arrange jacket part to obtain outer preform diameter of 30 mm. Also it keeps cladding and core part safe from any outer effects. Cladding part is formed of chalcogenide glass. Here we could use simply another polymer to see structural coloring effect but we choose to use chalcogenide glass due to its useful properties that will mentioned later in this work. Cladding part is the main part in which we observe structural coloring. As a core, again we use polymer. Polymer core provide us to have much longer nano-wires by supporting chalcogenide glass cladding part. Also it allows the formation of nano-sized tubes that we will mention in chapter 5 as future work. To obtain desired preform, we produce a polymer rod and a chalcogenide glass tube that has core diameter same as diameter of polymer rod. Then jacket part is obtained by polymer rolling and finally with the consolidation we will have our preform ready to use (Figure 3.3).

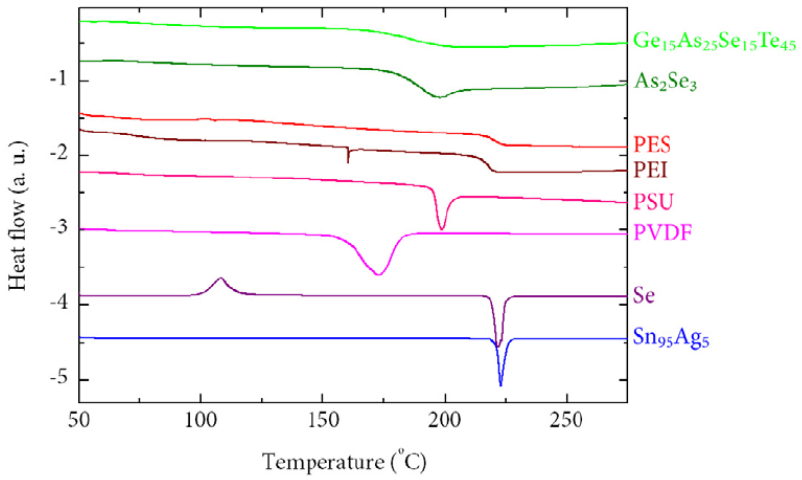

Figure 3.2: Dynamic Scanning Calorimetry (DSC) data shows the glass transition temperatures of materials used to draw fibers.

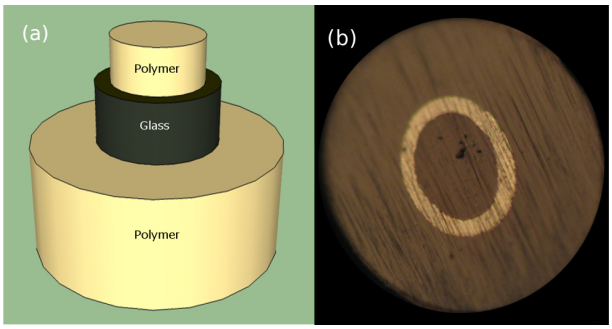

Figure 3.3: (a) Preform design (b) an optic microscopy image of produced preform.

3.1.2 Glass Tube Production

Chalcogenide glasses (Figure 3.5) have some superior properties as high refractive index, low phonon energy, high optical nonlinearity. In our work As_2Se_3 is chosen as a chalcogenide glass. The average refractive index of bulk As_2Se_3 in visible spectrum is measured as 3.25 by ellipsometer (Figure 3.4).

Due to its high refractive index As_2Se_3 is optically suitable material to observe structural coloring due to the resonant Mie scattering. Also for the future work as supercontinuum generation which will be explained in chapter 5, As_2Se_3 is an optimum material since it has one of the highest optical nonlinearity property.

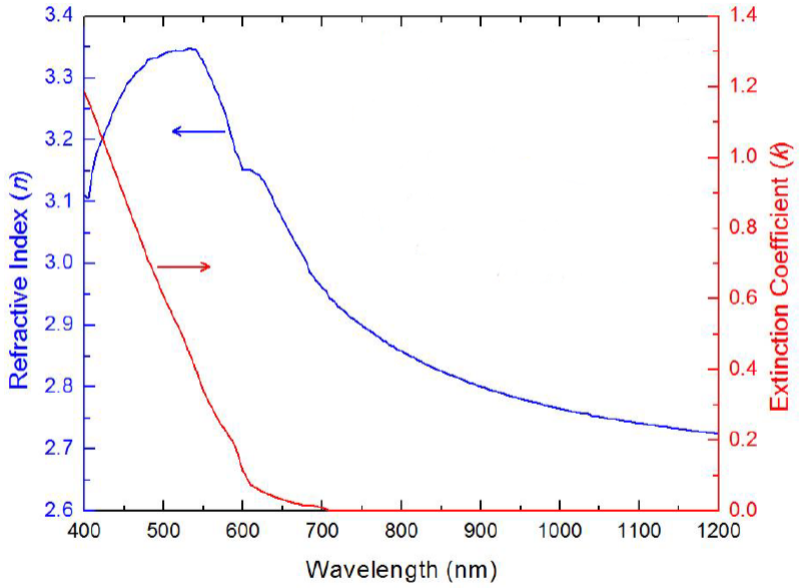

Figure 3.4: (n,k) values of As_2Se_3 measured by ellipsometer.

Bulk As_2Se_3 glass is first pulverized and after mass measurement, desired amount of material (25 gr in our case) is inserted into the quartz tube with appropriate diameter. Open end of the quartz tube is connected to a vacuum setup which consists of mechanical and turbo vacuum pumps. First, mechanical vacuum pump is operated to achieve vacuum in the range of 10^{-3} torr and As_2Se_3 is melted to get rid of extra volume by heating the quartz tube with the bunsen flame. Then, turbo pump is operated to achieve vacuum in the range of 10^{-6} torr. A liquid nitrogen trap placed before the inlet of turbo pump to protect its knives. When the whole vacuum system become static, bunsen flame is used to heat the quartz tube at a certain point close to the open end and stretching force is applied by pulling from the ends to seal the quartz tube by necking. At the end, quartz ampoule containing As_2Se_3 is obtained.

Obtained quartz ampoule is heated by the increment of 2°C per minute to 750°C and kept at this temperature over 10 hours in the furnace. Over-heated ampoule is rocked for 30 minute and fixed to a rotator machine (Figure 3.6) right after taking off the rocking furnace (Figure 3.7). Rotator machine rotates ampoule which contains melted As_2Se_3 around horizontal axis to have As_2Se_3 glass tube as it cooling down below melting point. After cooling, solid As_2Se_3

Figure 3.5: Pieces of chalcogenide glasses. Orange=As_2S_3 (Arsenic sulfide) Black=As_2Se_3 (Arsenic selenide).

tube extracted by breaking the quartz ampoule (Figure 3.8).

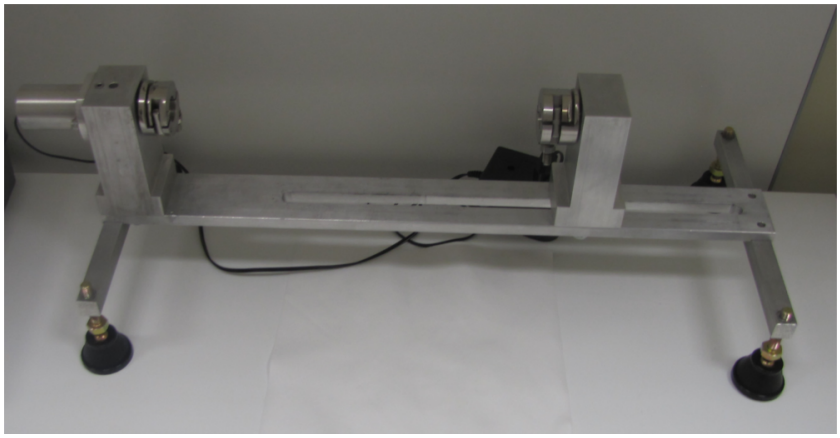

Figure 3.6: Rotator Machine.

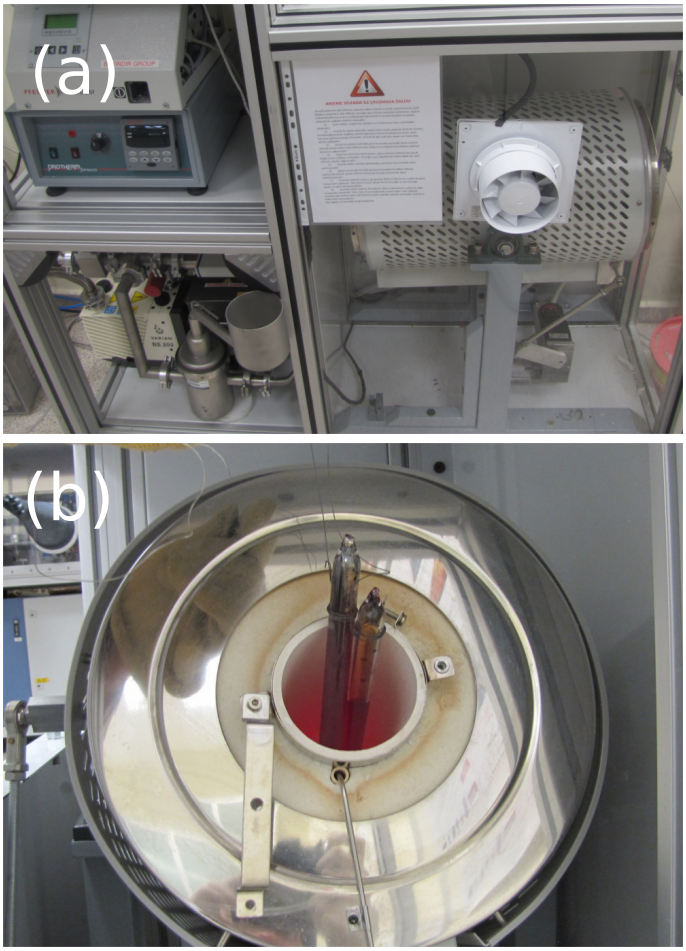

Figure 3.7: (a) Rocking furnace. (b) Quartz ampoule containing melted As_2Se_3.

3.1.3 Polymer Rolling and Consolidation

First, a teflon sheet that is cleaned by methanol is rolled around a cylindrical metal rod and fixed with vacuum tape to avoid polymer to stick metal rod when consolidating and also to obtain desired core diameter which is just enough for As_2Se_3 tube to enter. Then polymer sheet, PES in our case, is cleaned, prepared in desired sizes and kept one night in vacuum oven at 100°C to get rid of water vapour and then tightly rolled by hand around the metal rod that teflon sheet rolled onto it till reaching intended preform diameter. The last layer of polymer sheet is fixed with vacuum tape and whole preform is slightly covered with one layer of teflon band to avoid dirt. Prepared preform is placed in the consolidation

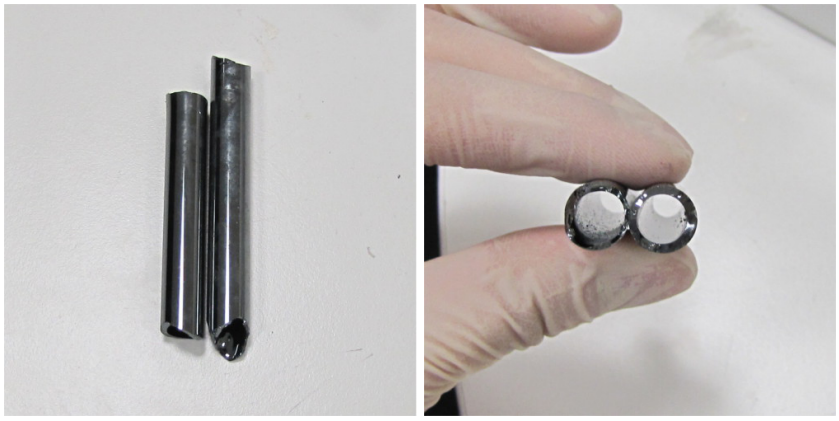

Figure 3.8: As_2Se_3 tubes after extracting from quartz ampoule.

furnace (Figure 3.9) and heated with 15°C per minute rate from room temperature to 180°C. After waiting 3 hours at 180°C, heating continued with 2°C per minute rate to 255°C and at this temperature, preform is kept 35 minutes and without waiting it to cool down slowly in the furnace, preform is removed and cooled down rapidly in room temperature. Rapid cool down is important to have materials in amorphous state. Then, the metal rod together with the teflon sheet is removed and As_2Se_3 glass tube placed at the core. Using extra, similarly prepared polymer (PES) preform, a polymer rod that has same diameter with inner diameter of As_2Se_3 glass tube is obtained at turning machine and placed at the core of As_2Se_3 glass tube. Finally, our preform is ready with intended design (Figure 3.10).

3.2 Production of Core-Shell Nano-Wires by ISR Technique

Thermal size reduction process is performed by using fiber tower (Figure 3.11) which basically consists of a tube furnace where its axis is positioned perpendicular to the ground, a stage to hang and to move preform, a capstan that provide the required uniform force to draw fiber and a computer that controls stage and capstan movements and shows data from sensors that measure thickness of fiber and pressure applied on fiber.

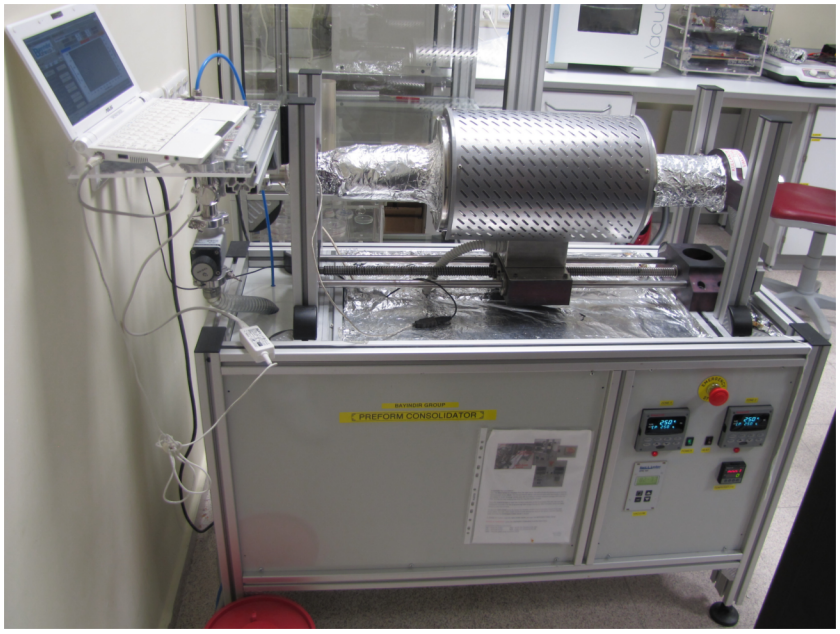

Figure 3.9: Consolidation Furnace.

Prepared preform is drilled from the ends through its diameter and one end is connected to an adapter that provides us to hang preform to the moving stage of the fiber tower. A mass is hanged to the other end to apply initial pulling force to start drawing process while capstan is not available to use. Then preform which is hanged to the moving stage of the fiber tower transferred into the furnace and centered. Open ends of furnace is closed to stabilize inside temperature. Furnace is heated to 180°C with 15°C per minute rate and without waiting, heating continued with 2°C per minute rate till drawing process starts. In our

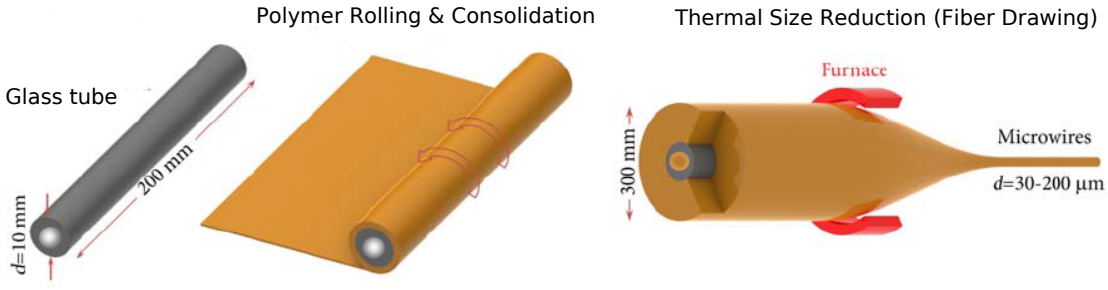

Figure 3.10: A model that shows polymer rolling & consolidation and fiber drawing processes.

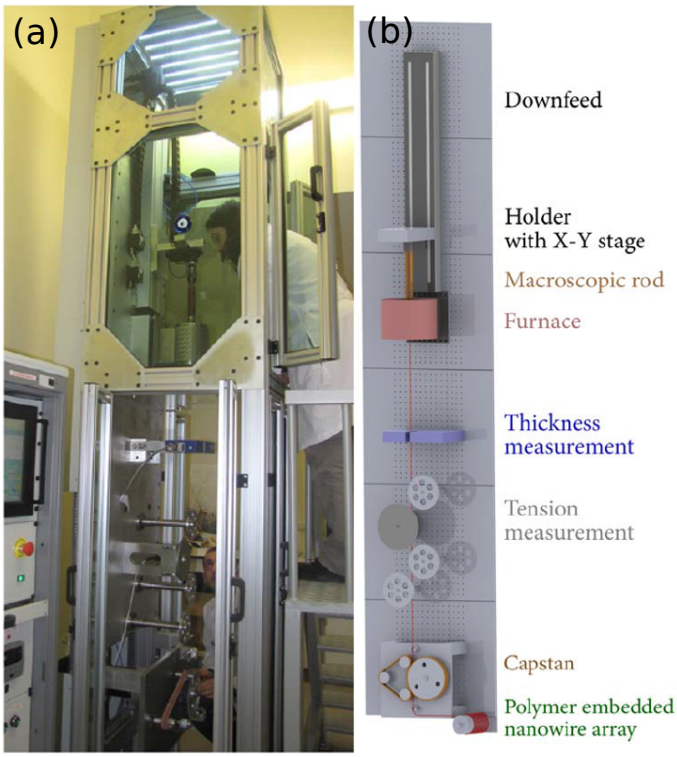

Figure 3.11: (a) A photograph of fiber tower.(b) A model that shows elements of fiber tower.

case drawing starts at 295°C. After drawing starts, we get rid of hanged mass and the end of the fiber is connected to capstan. To avoid to break fiber, the stage that holds preform is moved towards to ground with very low rates in the order of few millimeters per minute. Adjusting temperature and the velocity of the stage and the capstan, drawing process is continued with constant pressure so as to obtain fiber with uniform intended diameter.

After having first step fibers as described above, second step fibers are obtained by similar drawing process but this time when we prepare preform, instead of polymer core and glass cladding, we prepare a bundle of first step fibers and after polymer rolling and consolidation process we place that bundle into the core of preform. Then fiber drawing process performed to have second step fibers. Similarly third step fibers are obtained using a bundle of fibers from second step fibers. This method which is inspired by Taylor wire drawing process [49] is named as ISR process. [47] (Figure 3.12).

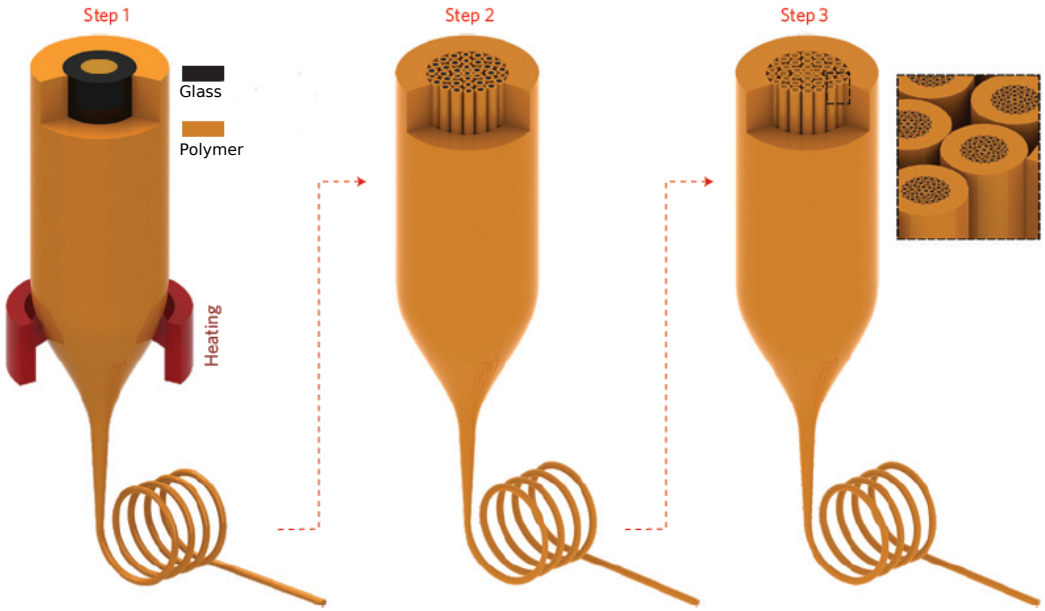

Figure 3.12: A model that shows iterative thermal size reduction technique.

3.3 Production of Core-Shell Nano-Spheres by in-Fiber Fluid Instability

In nature, everything tries to minimize its potential energy and in the case of fluid drops, the minimum energy state is a sphere since sphere comes with the minimum surface area and correspondingly the minimum surface potential energy due to the surface tension i.e. the Plateau-Rayleigh instability . Although our fibers are stable at room temperatures, when temperature is raised near melting point, they are instable because fiber drawing process is in high temperatures and then sudden cooling down of fibers in room temperature results a forced state [50] [51]. Since the melting point of the PES is higher then the melting point of As_2Se_3 glass, at the temperatures in between these two melting points, As_2Se_3 become fluid and tries to minimize its potential by forming spheres in the fiber (Figure 3.13).

In our case, because of our preform design, we have polymer also in the core. Therefore, when temperature is increased to a point between the melting points of polymer and As_2Se_3 using consolidation furnace, As_2Se_3 becomes fluid and

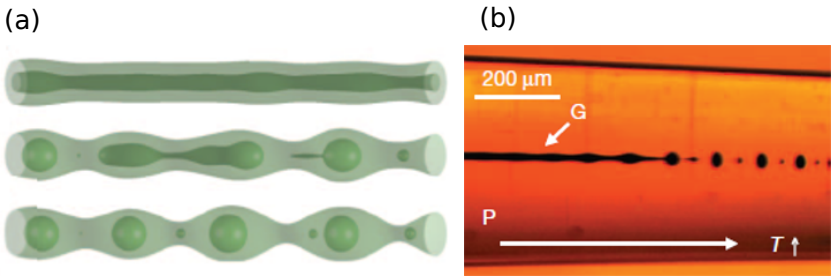

Figure 3.13: (a) A model that shows the process of obtaining spheres in-fiber by heating. (b) An actual fiber photograph which include spheres [50].

tries to form spheres but polymer, in the core, in fact it is softened but since it is not melted, resists the force that applied by As_2Se_3 glass to form spheres. If we try to exceed the melting temperature of polymer then fiber breaks. To observe this effect in our design we tried to expose fibers to a temperature around melting point of the polymer without exceeding it and we succeeded to obtain in-fiber spheres for second and third step fibers. Since the resisting force is higher for the first step fibers because of the larger sizes, we cannot have spheres for the first step fibers.

To obtain in-fiber spheres, two kind of samples are prepared. One of them is fixed with vacuum bands so it is not permitted to decrease in length while the other one is free standing. Spheres created by the fixed fiber have almost same diameters with the initial diameter of cladding and for the free standing fibers, spheres are formed with diameters almost two times bigger then the original cladding diameter.

3.4 Characterization of Nano-Structures

For samples from all three steps of fibers, chemical etching process is done using Dicloromethane (DCM) solution. DCM etches polymer while it is harmless to As_2Se_3 glass. Therefore, at the end, uniform As_2Se_3 glass tubes are expected to be obtained (Figure 3.14 and 3.17 3.25). Using resin solution with hardener solution together with amounts 15:1, a mixture is prepared, samples from all

three steps are embedded into this mixture and exposed to UV light source to solidify. Solidified samples are cut by microtome and cross-sections are imaged by SEM (Figure 3.15, 3.18 and 3.22). After obtaining in-fiber spheres from second and third steps, fibers are again buried to resin-hardener mixture and cut by microtome. Images that shows As_2Se_3 spheres encapsulating polymer core are taken by SEM (Figure 3.16, 3.19 and 3.23). Also etching process is done for second and third step fibers that have spheres and free standing spheres are imaged by SEM (Figure 3.20 and 3.24). Here is the results for all 3 steps.

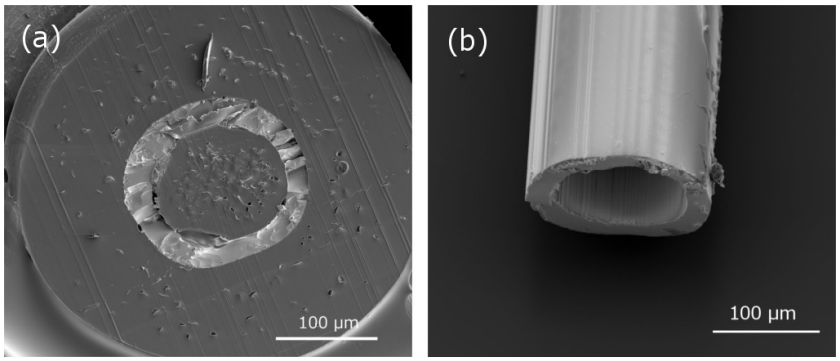

Figure 3.14: (a) SEM image of first step fiber after burying to resin and cutting by microtome. Polymer at the core and the jacket and tube chalcogenide glass are successfully obtained. (b) SEM image of first step fiber after chemical etching process. Chalcogenide glass tube is successfully obtained.

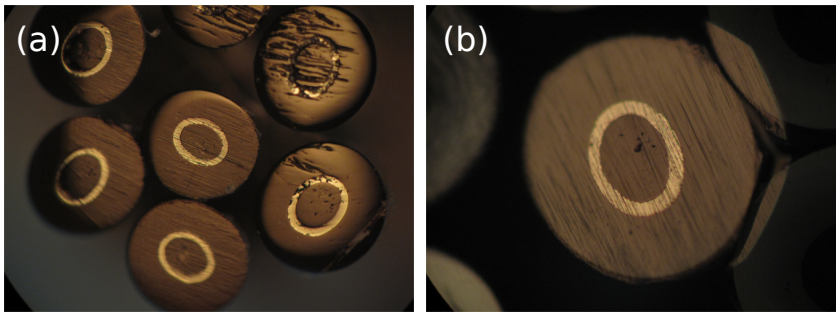

Figure 3.15: Optical microscopy image of (a) a bundle of first step fibers after rubbing with emery. (b) a first step fiber after rubbing with emery. Polymer at the core and the jacket and tube chalcogenide glass are successfully obtained.

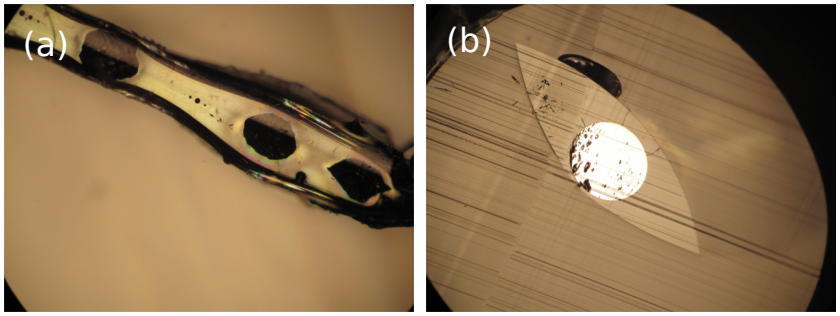

Figure 3.16: (a) Optical microscopy image of unsuccessful spheres obtained by fluid instability from heated first step fiber. Also some successful spheres are obtained. (b) Optical microscopy image of the successful spheres after burying to resin-hardener solution and cutting by microtome. Successful spheres are made of only chalcogenide glass without polymer in the core.

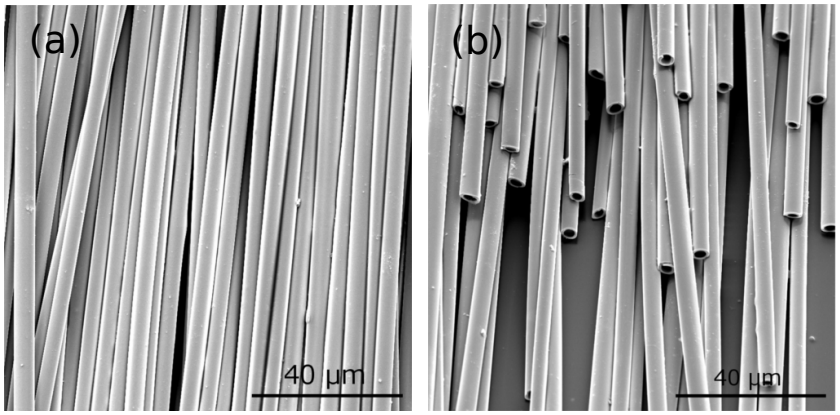

Figure 3.17: (a) SEM image of the second step fibers after chemical etching process. Uniformity of fibers are shown. (b) SEM image of the second step fibers as chalcogenide glass tubes after successful chemical etching process.

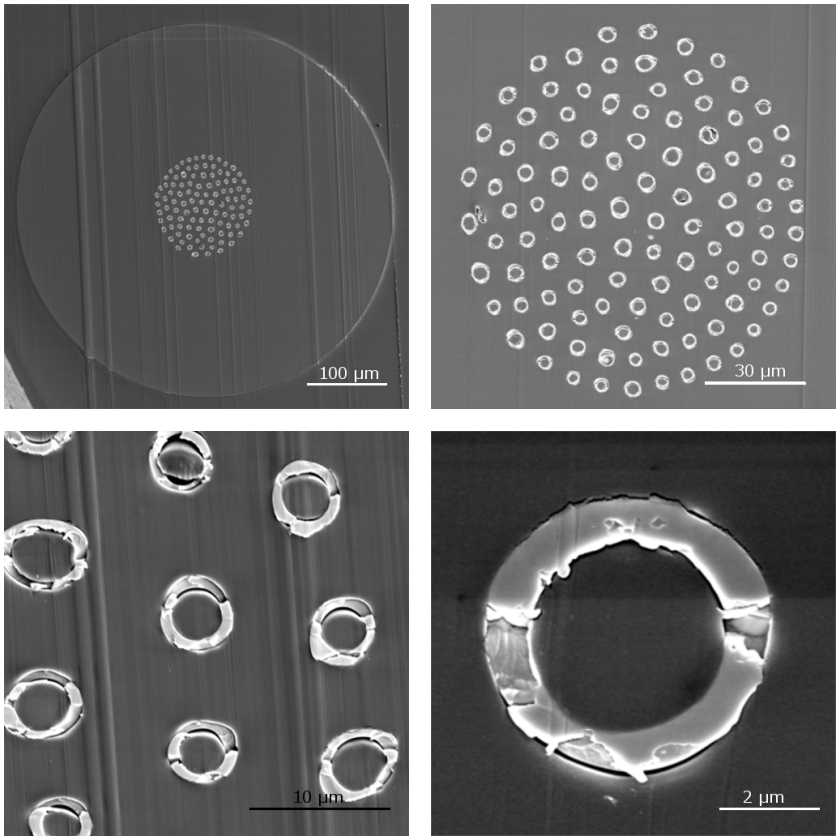

Figure 3.18: SEM image of the second step fiber with different magnifications after burying to resin-hardener solution and cutting by microtome. Uniformity of fiber array is shown.

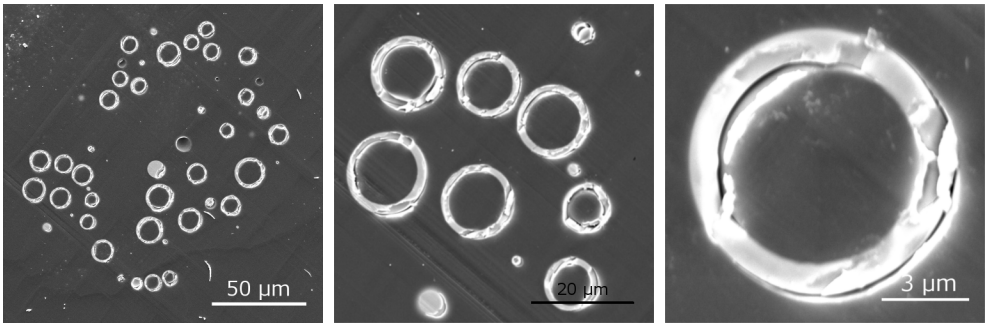

Figure 3.19: SEM images of the second step spheres obtained by in-fiber fluid instability process after burying to resin-hardener solution and cutting with microtome. Spheres that have polymer core which is encapsulated by chalcogenide glass are successfully obtained.

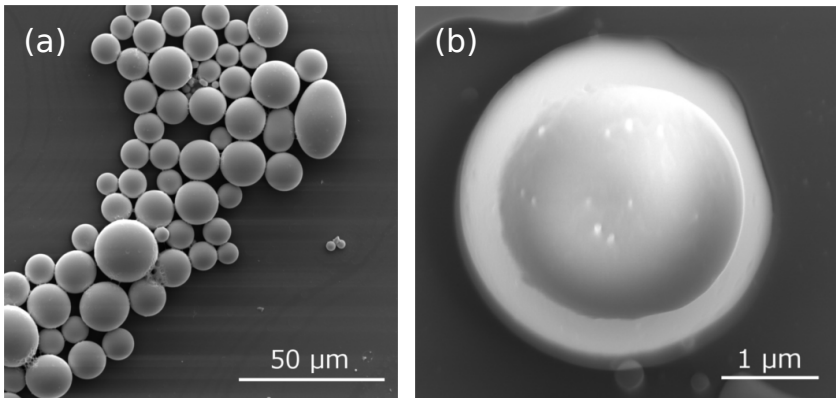

Figure 3.20: (a) SEM images of the second step spheres obtained by in-fiber fluid instability after chemical etching process. (b) SEM image of the second step sphere that has diameter less than 2 micrometers can show also the core polymer that is encapsulated by chalcogenide glass.

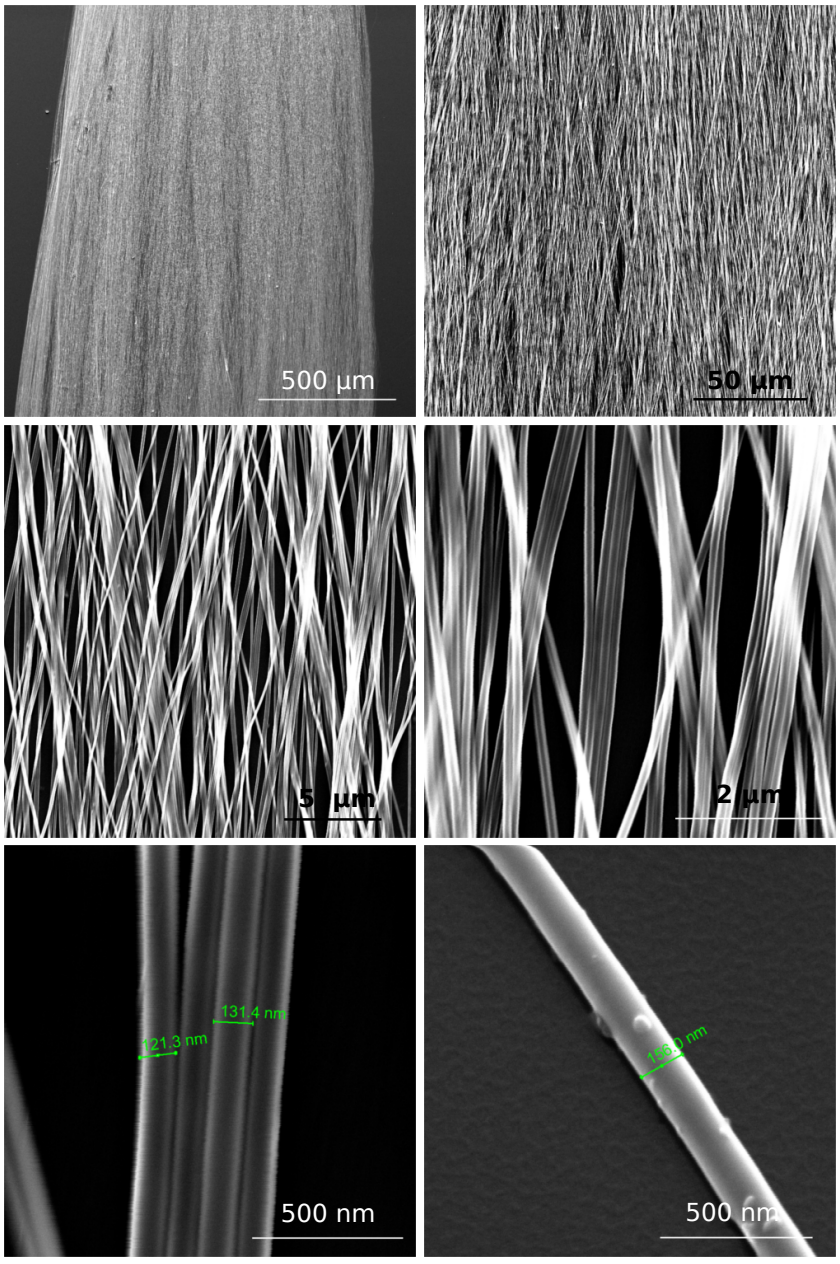

Figure 3.21: SEM images with different magnifications of third step fibers after chemical etching process. Uniformity is shown.

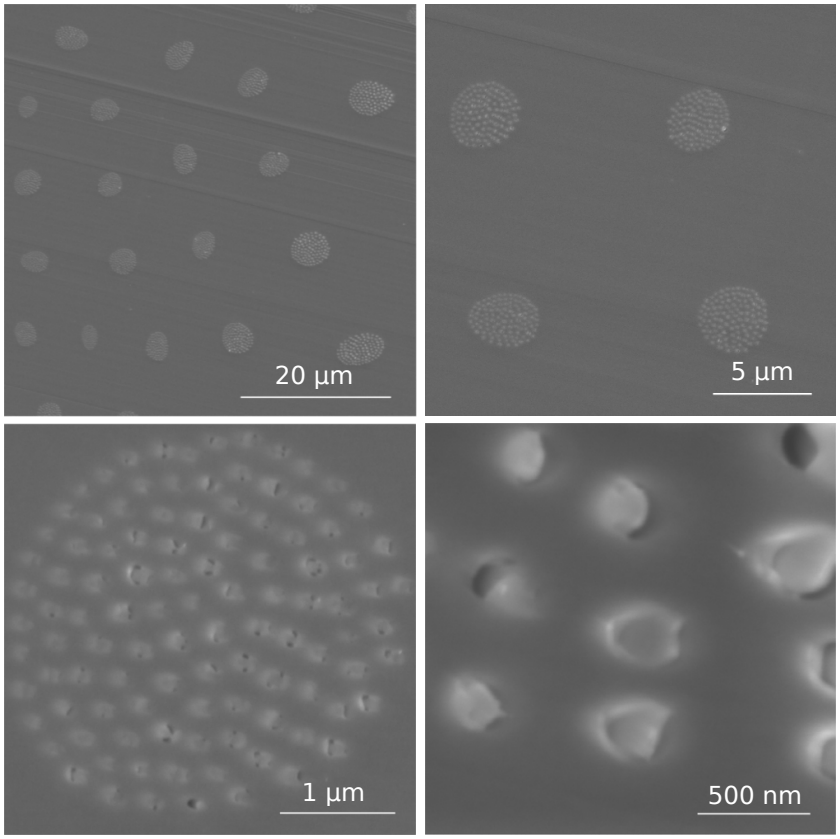

Figure 3.22: SEM image of the third step fiber with different magnifications after burying to resin-hardener solution and cutting by microtome. Uniformity of fiber array is shown.

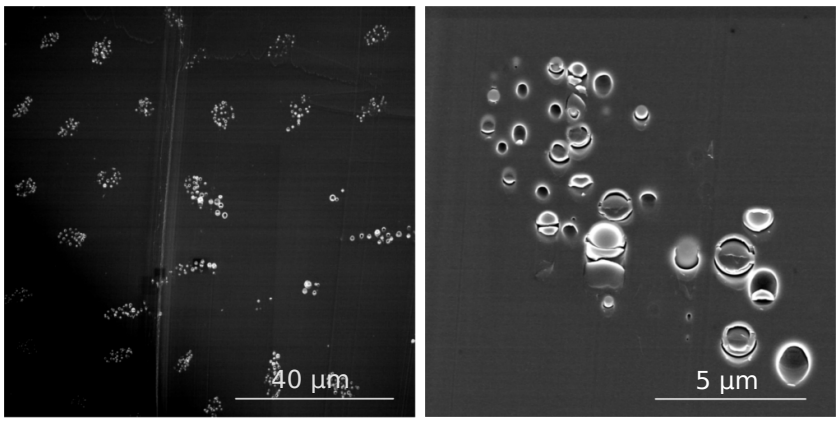

Figure 3.23: SEM images of the third step spheres obtained by in-fiber fluid instability process after burying to resin-hardener solution and cutting with microtome. Spheres that have polymer at the core which is encapsulated by chalcogenide glass are successfully obtained.

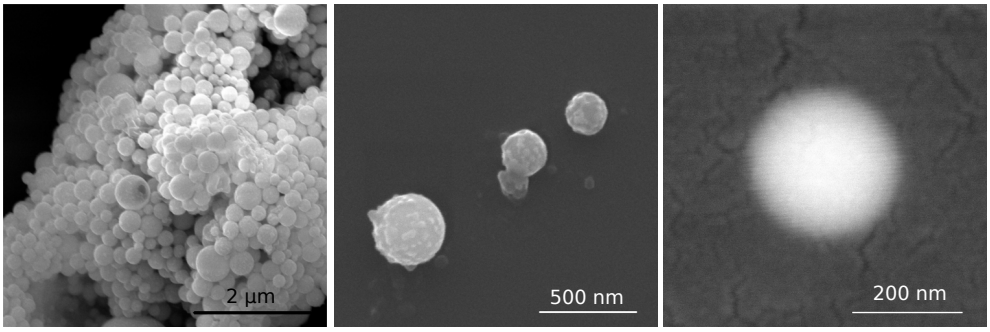

Figure 3.24: SEM images of the third step spheres obtained by in-fiber fluid instability after chemical etching process.

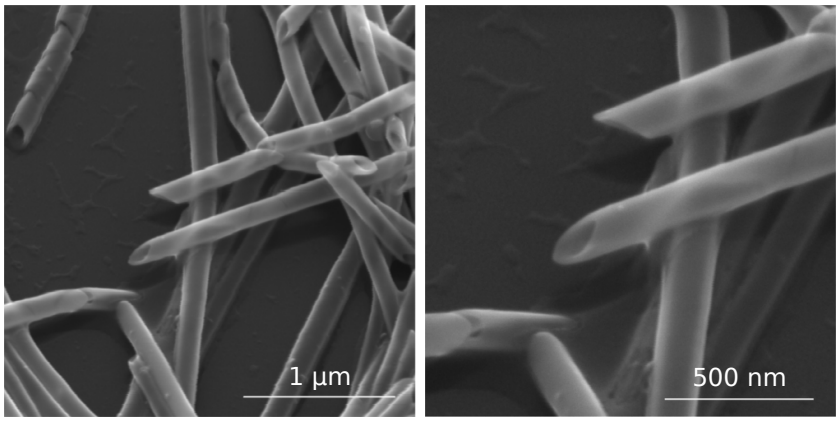

Figure 3.25: SEM images with different magnifications of the third step fibers as chalcogenide glass tubes after successful chemical etching process.

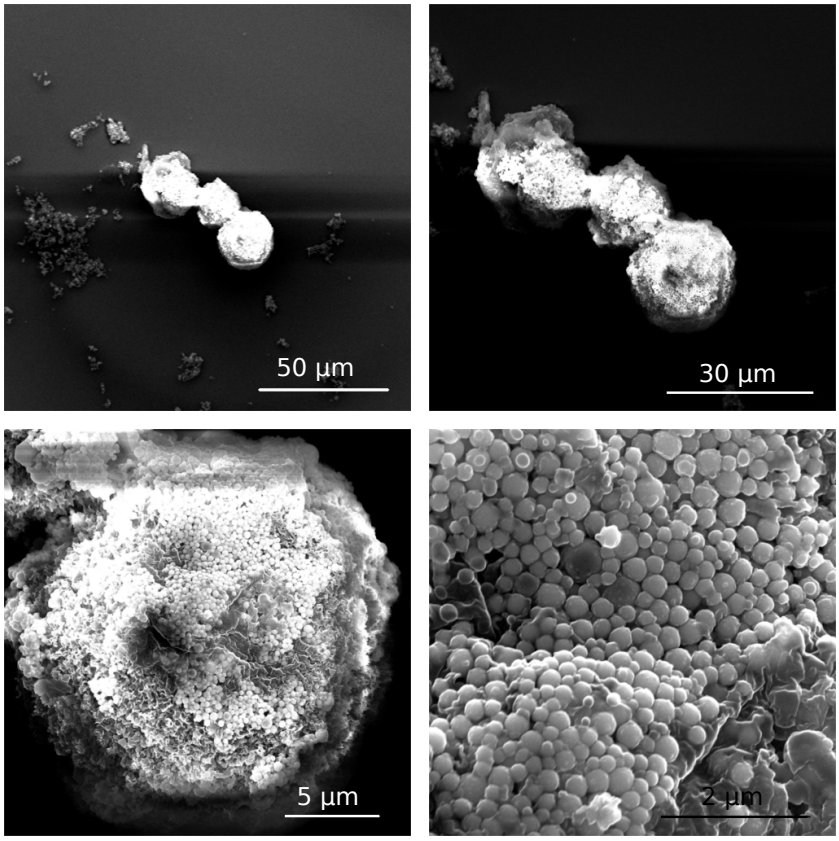

Figure 3.26: SEM images that shows interesting behaviour of third step spheres. Small spheres are hold on each other to form much bigger spheres.

Chapter 4

Scattering From Small Particles: Structural Coloration of Nano-Structures

4.1 Structural Coloration

Coloration not from light-dye interaction but from the diffraction of light from a material that has periodic or quasi-periodic structure in the scale of the wavelength of light is called structural coloration [52]. While in nature, structural coloration can be observed extensively as in mother-of-pearl, peacock feathers, many kind of bugs and birds [6] it can also be successively imitated in the laboratory with variety of methods [53] (Figure 4.1).

Structural colors are considered to originate light diffraction by thin film interference, multilayer interference, diffraction grating, photonic crystals and light scattering [4].

When light falls on to a thin film coating, structural colors are observed due to the interference of reflected light beam from air-film surface and film-based material surface constructively when $2n_2 dcos\theta_2 = m\lambda$ where n_2 is the refractive

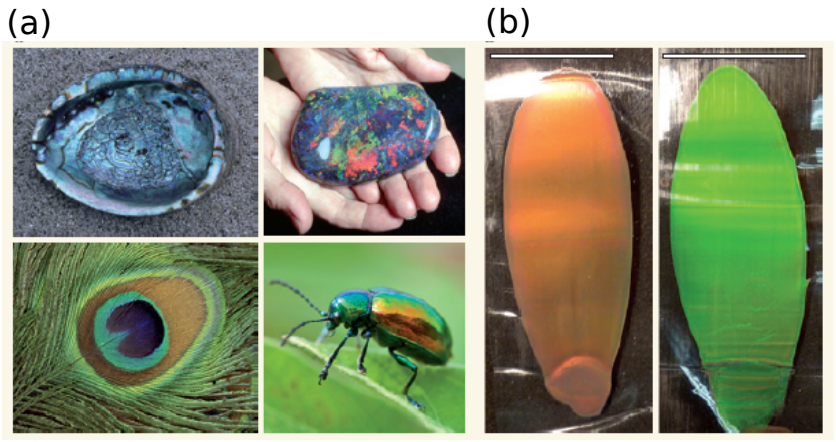

Figure 4.1: (a) Structural color in nature, mother of pearl, an opal, a peacock feather and a beetle (b) polymer films with structural colors created by edge induced rotational shearing by Finlayson et al. Scale bars are 3 centimeters [52].

index of film, d is the film thickness, θ_2 is the angle of refraction, m is an integer and λ is wavelength of light (Figure 4.2).

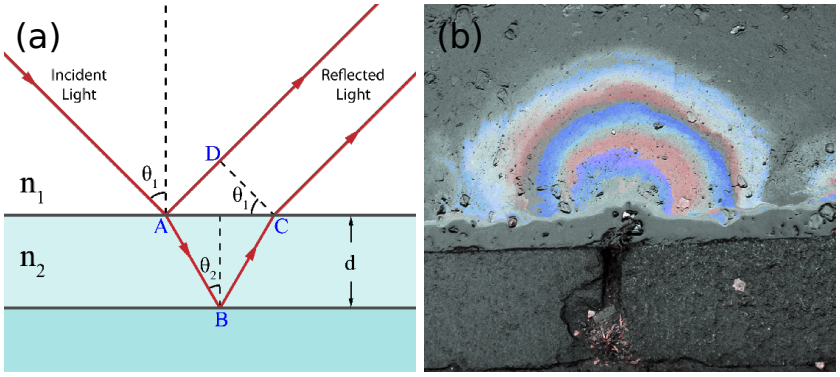

Figure 4.2: (a) scheme that illustrates thin film interference. (b) Structural coloration of oil layer on the water due to thin film interference.

If the coating is not a thin film coating but a multilayer coating which is an iterative coating of two different refractive index materials with two different thicknesses, similarly we see the structural coloration in the case of constructive interference if $2(n_A d_A cos\theta_A + n_B d_B cos\theta_B) = m\lambda$ (Figure 4.3).

Diffraction gratings which is commonly used in optics such as in monochromators, spectrometers and lasers, is an optical element that splits and diffract light because of its periodic structure. Structural colors are obtained because of

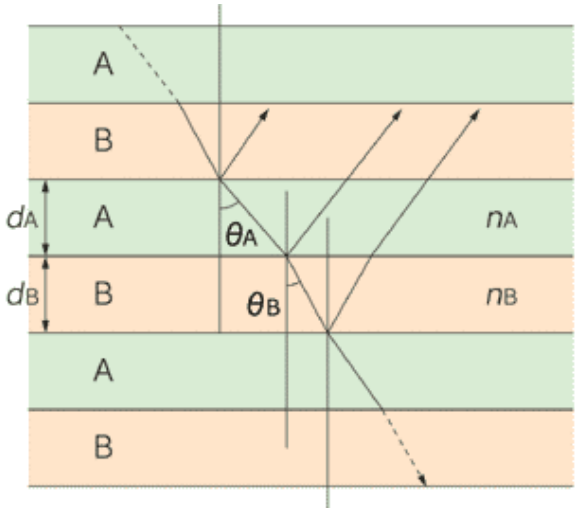

Figure 4.3: A scheme that illustrates multilayer interference.

diffraction of the light beams (Figure 4.4).

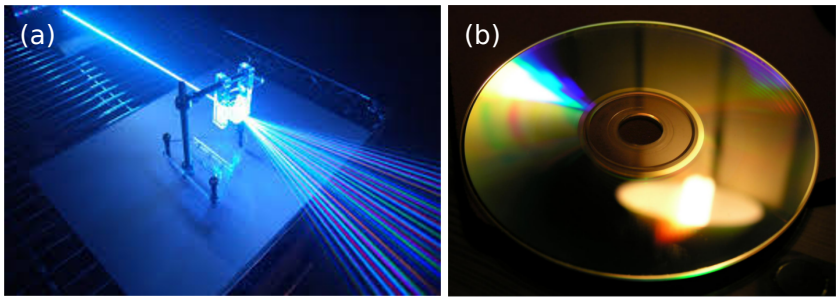

Figure 4.4: (a) Diffraction grating that splits light. (b) The compact disc can act as a grating and produce iridescent reflections.

Another component that creates structural coloration is photonic crystals. A phonic crystal is a periodic optical nano-structure in 1D, 2D or 3D that affects the motion of photons in the similar manner with ionic lattices that effects motion of electrons (Figure 4.5).

The last known method related to the structural coloration is light scattering from materials with the sizes comparable to the wavelength of light. In chapter 2 and the following sections of this work this method is widely described.

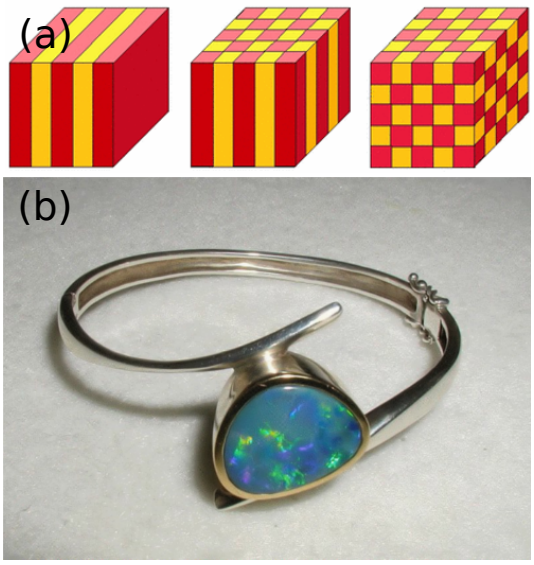

Figure 4.5: (a) Illustration 1D,2D and 3D photonic crystals [54] (b) An opal that is a natural phonic crystal.

4.2 Analytical Solutions: Mie Theory

The scattering efficiency for light is defined as [36]

$$Q_{sca}(x) = \frac{1}{x}\sum_{n=-\infty}^{\infty}(|a_n^2| + |b_n^2|) \tag{4.1}$$

where a_n and b_n are scattering coefficients which we can estimate for nanospheres by solving the 8 equations in chapter 2 from Equation 2.80 to Equation 2.87. For simplicity we took $\mu = \mu_1 = \mu_2$.

$$a_n = \frac{\psi_n(y)[\psi_n'(m_2y) - A_nX_n'(m_2y)] - m_2\psi_n'(y)[\psi_n(m_2y) - A_nX_n(m_2y)]}{\xi_n(y)[\psi_n'(m_2y) - A_nX_n'(m_2y)] - m_2\xi_n'(y)[\psi_n(m_2y) - A_nX_n(m_2y)]} \tag{4.2}$$

$$b_n = \frac{m_2\psi_n(y)[\psi_n'(m_2y) - B_nX_n'(m_2y)] - \psi_n'(y)[\psi_n(m_2y) - B_nX_n(m_2y)]}{m_2\xi_n(y)[\psi_n'(m_2y) - B_nX_n'(m_2y)] - \xi_n'(y)[\psi_n(m_2y) - B_nX_n(m_2y)]} \tag{4.3}$$

where

$$A_n = \frac{m_2\psi_n(m_2x)\psi_n'(m_1x) - m_1\psi_n'(m_2x)\psi_n(m_1x)}{m_2X_n(m_2x)\psi_n'(m_1x) - m_1X_n'(m_2x)\psi_n(m_1x)} \tag{4.4}$$

$$B_n = \frac{m_2\psi_n(m_1x)\psi_n'(m_2x) - m_1\psi_n(m_2x)\psi_n'(m_1x)}{m_2X_n'(m_2x)\psi_n(m_1x) - m_1X_n(m_2x)\psi_n'(m_1x)} \tag{4.5}$$

Scattering efficiency for nano-spheres (Figure 4.6) estimated using MATLAB code attached to the appendix. For core radius equal or smaller than 25nm, there is no coloration. Between 30 nm to 60 nm almost all visible spectrum scanned and from 60 nm to 112.5 nm, dominating color is red. Since our average spheres has 100 nm core radius. We expect to see dominating red color.

Scattering coefficients for nano-wires follows. Here $|a_n^2|$ presents TE polarization case while $|b_n^2|$ presents TM polarization case and $|a_n^2| + |b_n^2|$ term in the scattering efficiency belongs to unpolarized light.

$$a_n = \frac{J_n'(y)D_1 - J_n(y)C_1}{H_n'^{(1)}(y)D_1 - H_n^{(1)}(y)C_1} \tag{4.6}$$

$$b_n = \frac{J_n'(y)C_2 - J_n(y)D_2}{H_n'^{(1)}(y)C_2 - H_n^{(1)}(y)D_2} \tag{4.7}$$

where

$$C_1 = m_2Y_n'(ym_2) + m_2\frac{Y_1}{J_1}J_n'(ym_2) \tag{4.8}$$

$$D_1 = m_2^2Y_n(ym_2) + m_2^2\frac{Y_1}{J_1}J_n(ym_2) \tag{4.9}$$

$$C_2 = m_2J_n(ym_2) + m_2\frac{J_2}{Y_2}Y_n(ym_2) \tag{4.10}$$

$$D_2 = m_2^2J_n'(ym_2) + m_2^2\frac{J_2}{Y_2}Y_n'(ym_2) \tag{4.11}$$

where

$$J_1 = m_1 J_n(xm_1) J'_n(xm_2) - m_2 J_n(xm_2) J'_n(xm_1) \tag{4.12}$$

$$Y_1 = m_2 Y_n(xm_2) J'_n(xm_1) - m_1 J_n(xm_1) Y'_n(xm_2) \tag{4.13}$$

$$J_2 = m_2 J_n(xm_2) - \frac{m_2^2}{m_1} J_n(xm_1) \frac{J'_n(xm_2)}{J'_n(xm_1)} \tag{4.14}$$

$$Y_2 = \frac{m_2^2}{m_1} J_n(xm_1) \frac{Y'_n(xm_2)}{J'_n(xm_1)} - m_2 Y_n(xm_2) \tag{4.15}$$

Scattering efficiency for nano-wires due to TE, TM polarized (Figure 4.7) and unpolarized (Figure 4.8) light cases are estimated using MATLAB code attached to the appendix. For TE polarized light, at 25 nm core radius there is no clear coloration, at 50 nm and 75 nm core radius there is linearly decreasing scattering efficiency behavior from violet to red colors so dominating color is violet, at 100 nm core radius scattering efficiency for violet is also decreasing and dominating color shifted to light blue-green color. For TM polarized light, at 25 nm and 50 nm core radiuses scattering efficiency is dominated by red color. At 75 nm and 100 nm core radius while dominating peak goes off to the visible spectrum from red side, secondary dominating peak determines color from all spectrum. For unpolarized light, at 25 nm and 50 nm core radius red color dominates, at 75 nm and 100 nm core radius again highest peak stands at reddish colors but scattering efficiency for other colors are also strong. Since our nano-wires has radius between 50 nm and 75 nm, we expect to see every color but red color intensity must be stronger.

4.3 Numerical Calculations Based on Finite Difference Time Domain Simulations

Using FDTD method, scattering efficiency is simulated for both nano-wire (Figure 4.9) and nano-sphere (Figure 4.10) cases. For nano-wires, we expect to have stronger scattering efficiency in TM case from our estimations by MATLAB and in the FDTD simulations we achieved the same result. Similar to MATLAB results, for TM polarized light, scattering efficiency is initially dominated by red color with increasing core radius while for TE case dominating color initially was violet. As we expect, dominating peak goes off to the visible spectrum from red side for TM case and then secondary dominating peak scans other colors and for TE case we stars to see all colors with comparable scattering efficiencies for increasing core radius values.

For nano-spheres, results are also similar with MATLAB results. For core radius values smaller than 30 nm there is no coloration. From 30 nm to 100 nm all visible spectrum scanned from violet to red by first dominating scattering efficiency peak and when it goes off from the red side, secondary dominating peak scans visible spectrum from 100 nm to 150 nm. Since our average sized spheres has 100 nm radius, we expect to see dominating red color.

4.4 Observation of Structural Coloration in Large-Area Nano-Wires and Nano-Spheres

Structural coloration can be observed in third step fibers even without microscopy. Right after fiber drawing process, first and second step fibers did not change their colors but third step fibers become reddish (Figure 4.11). When chemical etching process takes place, optical microscopy images of third step fibers are taken. Coloration is observed both from bundle (Figure 4.13) and from single standing nano-wires (Figure 4.12). Also third step fibers are exposed temperature to obtain third step spheres. Since during the heating process diameters of spheres increases

nearly two times of original fiber diameters, colors from smaller sizes are lost. Decreasing sizes cause structural coloration to shift to violet side while increasing sizes cause shifting to red side. Therefore our third step spheres are shifted to red side and only red color is observed as expected from MATLAB and FDTD simulation results (Figure 4.14).

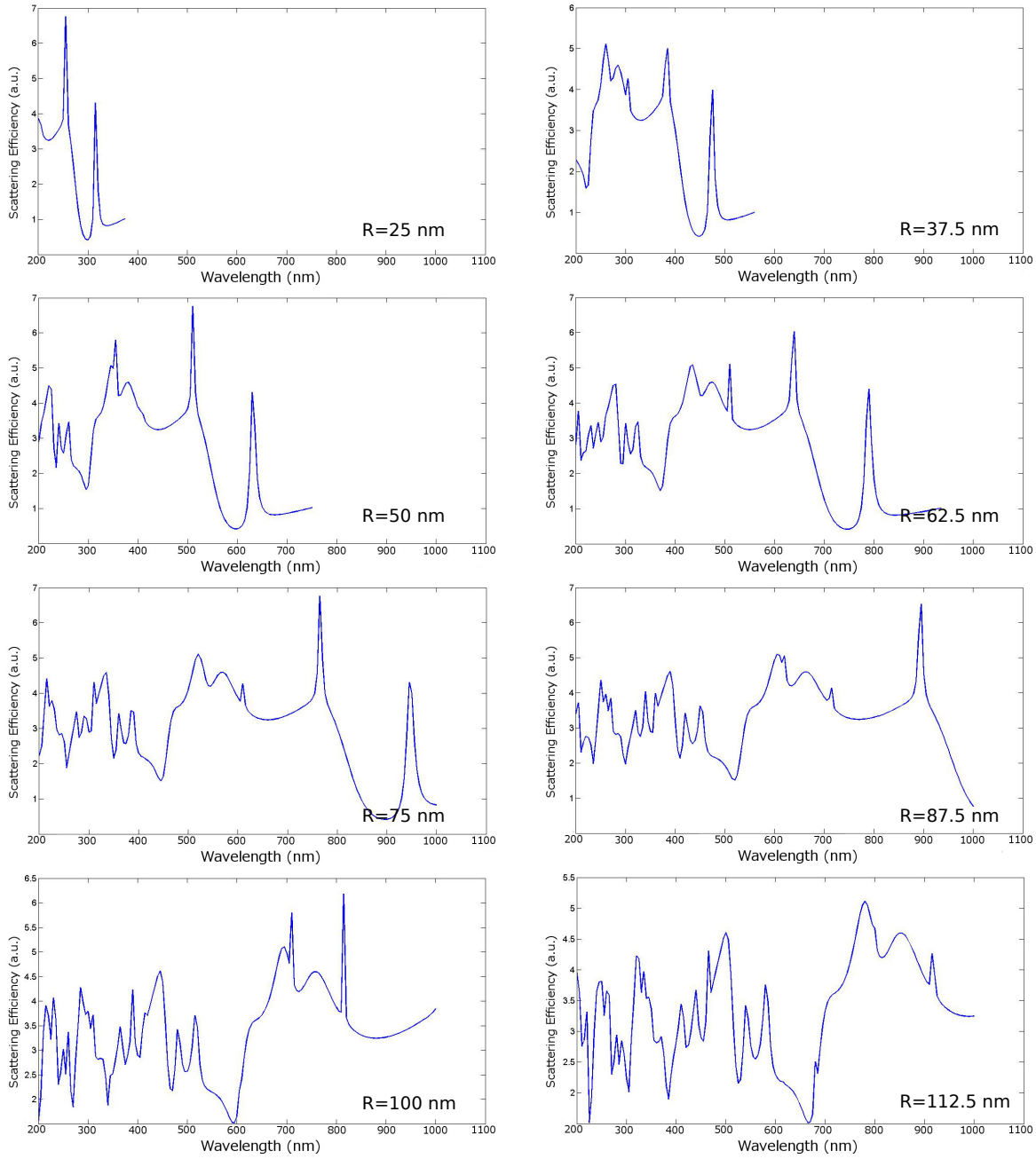

Figure 4.6: Graphics showing scattering efficiency and wavelength relation for different core radius values of nano-spheres. For core radius equal or smaller than 25 nm, there is no coloration. Between 30 nm to 60 nm almost all visible spectrum scanned and from 60 nm to 112.5 nm, dominating color is red.

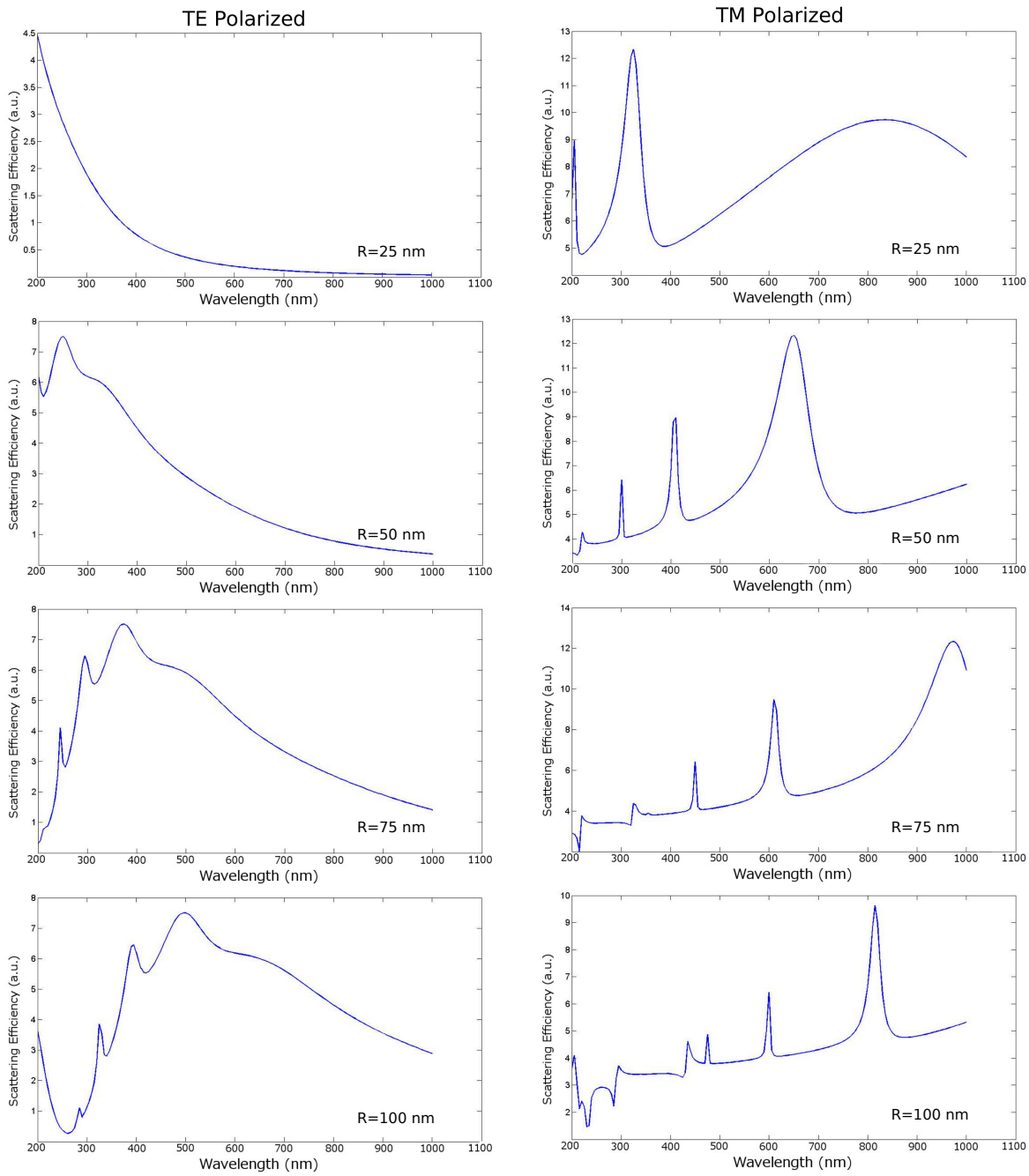

Figure 4.7: Graphics showing scattering efficiency and wavelength relation for different core radius values of nano-wires in both TE and TM polarized light cases.

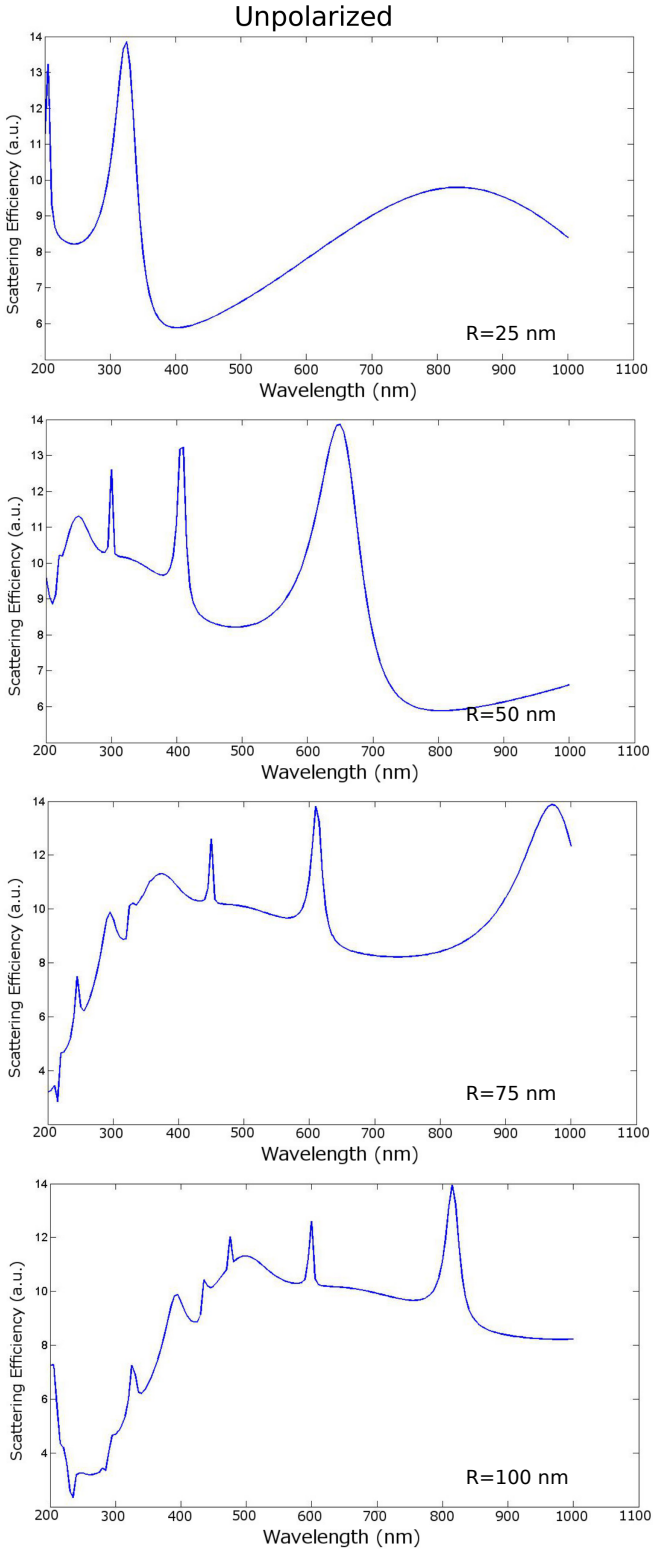

Figure 4.8: Graphics showing scattering efficiency and wavelength relation for different core radius values of nano-wires in unpolarized light case.

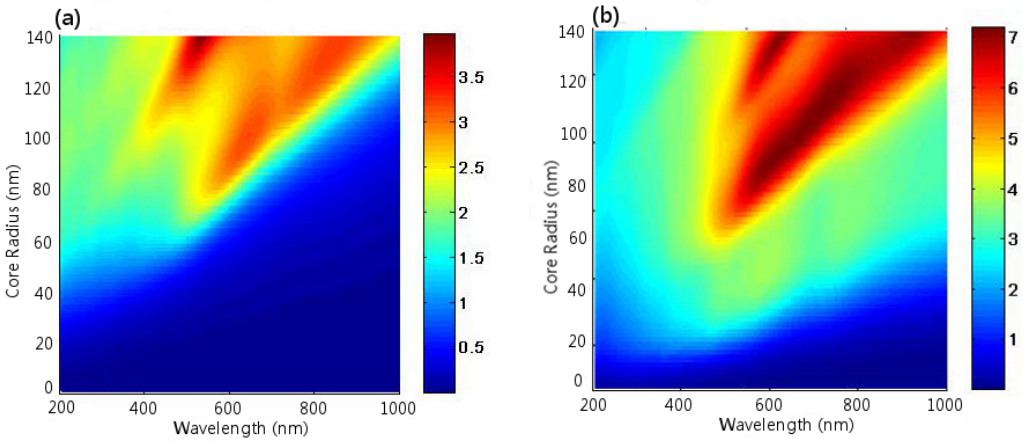

Figure 4.9: FDTD simulation results for nano-wires in TE and TM polarized light case. Results are similar with MATLAB results.

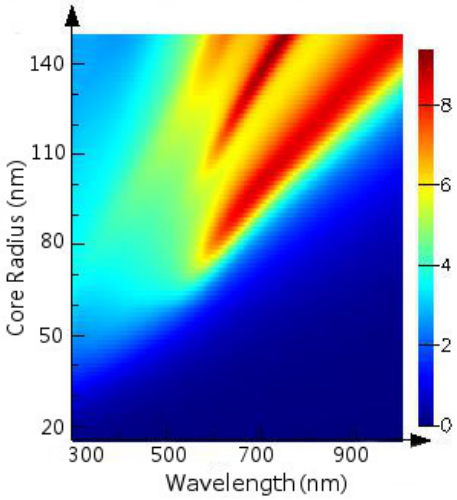

Figure 4.10: FDTD simulation results for nano-spheres. Results are similar with MATLAB results.

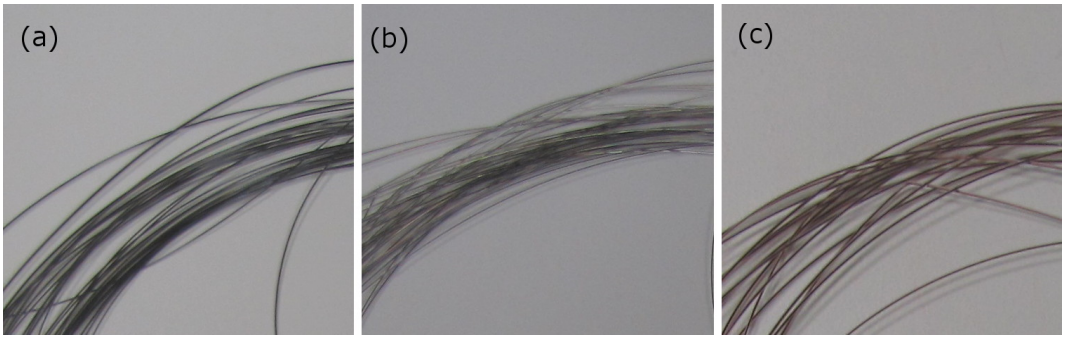

Figure 4.11: Bare fibers after fiber drawing process. (a) First step fibers. (b) Second step fibers. (c) third step fibers. Coloration of third step fibers can be observed even with bare eye.

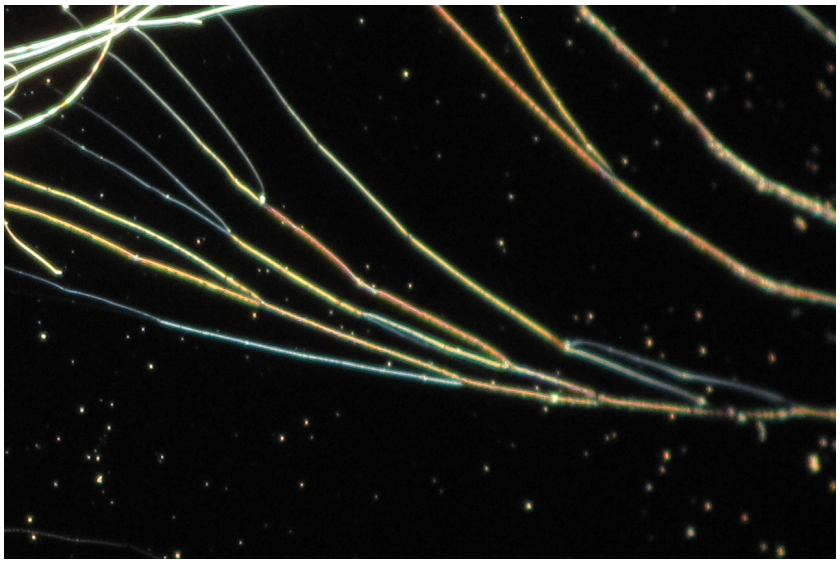

Figure 4.12: An image shows structural coloration from single standing third step fibers. All colors can be seen.

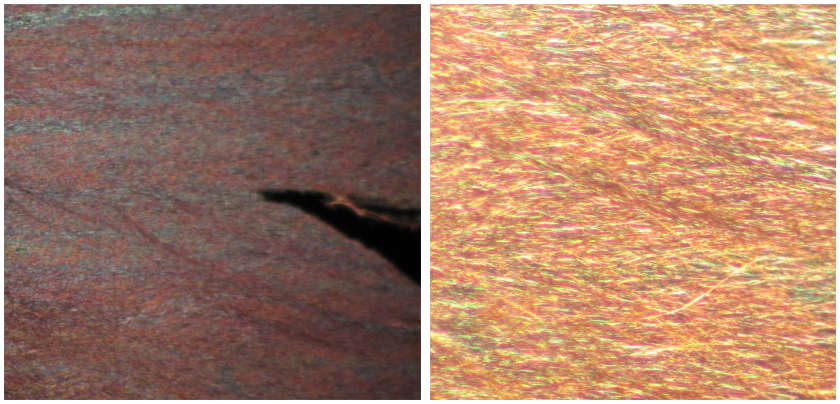

Figure 4.13: An image shows structural coloration from bundle of third step fibers. While dominating color is red, all colors can be seen as expected.

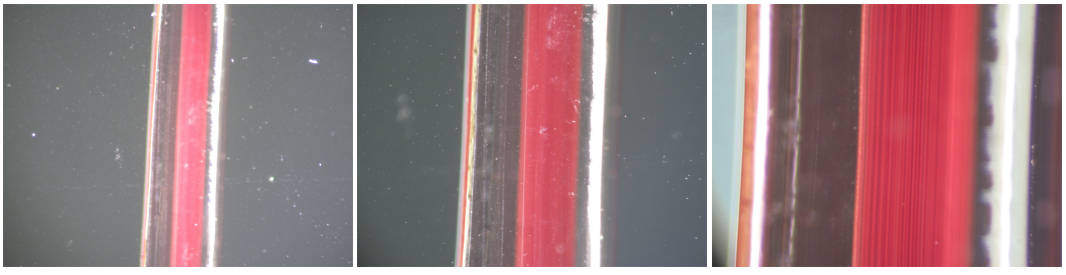

Figure 4.14: An image shows in-fiber structural coloration of third step spheres with different magnifications. Dominating red color can be seen.

Chapter 5

Summary and Outlook

Present work includes novel methods to produce nano-structures and theoretical background and observation of structural coloration based on scattering of light from produced structures in sizes comparable with the wavelength of light. Theoretical work is done by solving the wave equation to describe initial, internal and scattering electromagnetic fields for a linear, isotropic and homogeneous medium in cylindrical and spherical geometries. Structural coloration is observed for nano-structures in the form of core-shell nano-wires and nano-spheres that are produced by ISR and in-fiber fluid instability based on Plateau-Rayleigh instability methods.

Uniform and size controlled kilometers of long core-shell nano-wires are produced by a novel production method, ISR. First a cylindrical preform is prepared using polyether sulfone (PES) polymer rod in the core, As_2Se_3 chalcogenide glass tube as a cladding part and again PES polymer as an encapsulation jacket. After consolidation process preform is drown at the fiber tower to obtain first step fibers. A second preform is prepared using a bundle of first step fibers as a core and PES as an encapsulation jacket. Second step fibers are obtained by drawing the second preform and similarly a bundle of second step fibers used to obtain third step fibers. Reducing the size with three steps and getting rid of the encapsulation jacket by chemical etching with dicloromethane (DCM) solution, polymer core chalcogenide glass fibers with average diameter of 130nm are

obtained. Fibers are characterized by both longitudinal and cross-section images by scanning electron microscopy (SEM).

Sample fibers from all three steps are exposed to temperature near the melting temperature of As_2Se_3 chalcogenide glass. Based on the Plateau-Rayleigh instability effect, melted glass tries to form spheres inside the fibers. For second and third steps, chalcogenide glass spheres encapsulating polymer core are obtained but for the case of first step fibers, because of larger diameters compared to other steps, glass cannot apply enough force to the core polymer and successful spheres cannot be obtained. Spheres are characterized taking free standing and cross-section images by scanning electron microscopy (SEM).

Based on the theoretical calculations, MATLAB code that estimates the scattering behaviour of nano-wires and nano-spheres is written. Results are compared to the FDTD (Finite Domain Time Difference) simulations. As expected from theoretical results and simulations, structural coloration of nano-wires and nano-spheres are observed by dark field optical microscopy images.

5.1 Future Works

Microchannel Plate Detectors

A microchannel plate detector is a component used in detection of particles that multiplies photons as in photomultiplier tubes. The basic element of device is microchannel plate which is made from highly resistive material of nearly 2 mm thickness with regular array of densely distributed microchannels lying from one face to other (Figure 5.1). Then a layer of material that has high secondary electron emission [55] as magnesium oxide (MgO), beryllium oxide (BeO) or gallium phosphide (GaP) is coated in the microchannels by ALD (Atomic Layer Deposition) method. When a photon rips an electron from material and by applied voltage difference causes electric field along microchannels, ripped electron is accelerated through microchannels colliding with inner surface and for each collision electron rips other electrons due to the secondary electron emission

property of coated material. This process iteratively continue to the other side of the microchannel and around 10^6 gain obtained. Finally using phosphor screen, multiplied photons obtained by multiplied electrons [56].

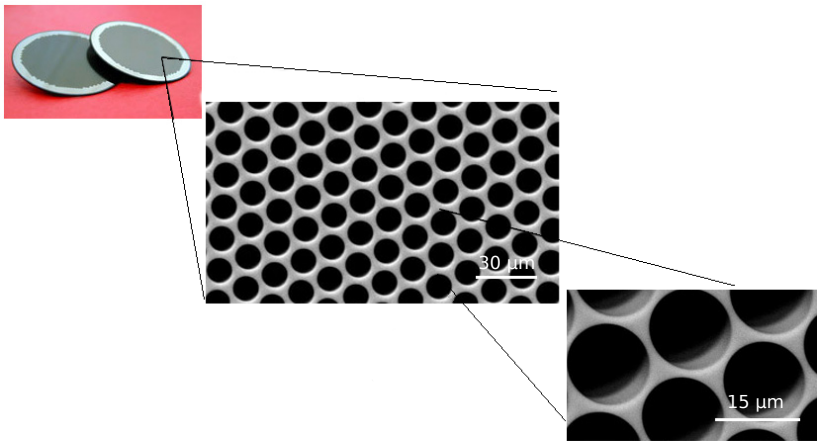

Figure 5.1: An image showing microchannel plate with different magnifications.

ISR technique provides the ability to produce uniform, cheap, long and controllable sized fiber arrays. Also our work proved that chemical etching of polymer with diclorometha ne solution is achieved even for third step fibers that has nearly 100nm polymer core radius. Based on these results, production of microchannel plates can be accomplished by appropriate design and materials. For instance, first step fibers can be obtained using PVDF (Polyvinylidene Fluoride) polymer which is not effected by diclorometha ne solution as a thin cladding and PC (Polycarbonate) polymer in the core. Second step fibers can be obtained using first step fibers in the core and PVDF polymer as a thin cladding and similarly after producing third step fibers we can obtain fiber arrays with intended fiber sizes due to the size reduction factor that we can control. A bundle of third step fibers can be consolidated and with chemical etching microchannel plate design can be achieved.

Supercontinuum Generation

Supercontinuum generation is simply a broadening of a pump beam by a collection of nonlinear effects (Figure 5.2 and 5.3). Chalcogenide glasses have

high nonlinear effects and supercontinuum generation can be achieved in tapered chalcogenide glass core-shell fibers [57] [58] [59]. Second or third step fibers produced by ISR technique can be used as an alternative way to tapering mechanism and since ISR results not only fiber but fiber arrays, stronger supercontinuum effect can be obtained.

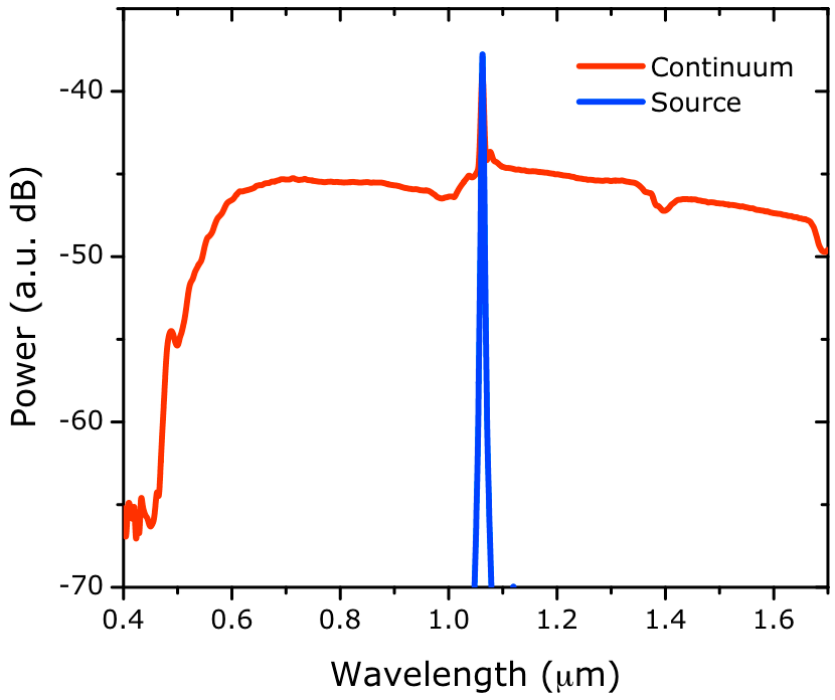

Figure 5.2: A typical supercontinuum spectrum. The blue line is the spectrum of the pump source while the red line is the resulting broadened spectrum generated after propagating through the fiber.

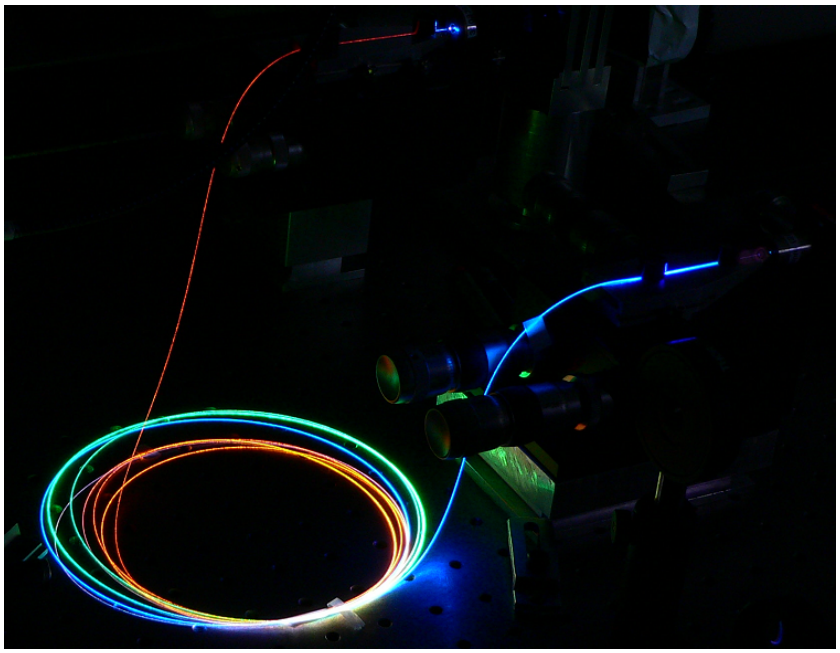

Figure 5.3: An image that shows propagation of laser pulses in a micro-structured optical fiber. The input is near infrared laser light is not visible before entry into the fiber and generates wavelengths covering the visible spectrum.

Bibliography

[1] C. F. Bohren, "Understanding colors in nature," *Pigm. Cell Res.*, vol. 1, no. 4, pp. 214–222, 1988.

[2] B. A. McRae, "Colors from nature: growing, collecting, and using natural dyes.," 1993.

[3] H. Zollinger, *Color chemistry: syntheses, properties, and applications of organic dyes and pigments*. Wiley. com, 2003.

[4] S. Kinoshita and S. Yoshioka, "Structural colors in nature: the role of regularity and irregularity in the structure," *ChemPhysChem*, vol. 6, no. 8, pp. 1442–1459, 2005.

[5] S. Kinoshita, S. Yoshioka, and J. Miyazaki, "Physics of structural colors," *Rep. Prog. Phy.*, vol. 71, no. 7, p. 076401, 2008.

[6] S. Kinoshita, *Structural colors in the realm of nature*. World Scientific, 2008.

[7] G. r. Tayeb, B. Gralak, S. Enoch, *et al.*, "Structural colors in nature and butterfly-wing modeling," *Opt. Photonics News*, vol. 14, no. 2, pp. 38–43, 2003.

[8] H. Cong and W. Cao, "Thin film interference of colloidal thin films," *Langmuir*, vol. 20, no. 19, pp. 8049–8053, 2004.

[9] R. W. Phillips, S. P. Fisher, and P. G. Coombs, "High chroma multilayer interference platelets," Nov. 5 1996. US Patent 5,571,624.

[10] B. Gralak, G. Tayeb, and S. Enoch, "Morpho butterflies wings color modeled with lamellar grating theory," *Opt. Express*, vol. 9, no. 11, pp. 567–578, 2001.

[11] J. D. Joannopoulos, S. G. Johnson, J. N. Winn, and R. D. Meade, *Photonic crystals: molding the flow of light*. Princeton university press, 2011.

[12] N. I. Zheludev, "What diffraction limit?," *Nat. Mater.*, vol. 7, no. 6, pp. 420–422, 2008.

[13] D. K. Gramotnev and S. I. Bozhevolnyi, "Plasmonics beyond the diffraction limit," *Nat. Photonics*, vol. 4, no. 2, pp. 83–91, 2010.

[14] H. C. Hulst and H. C. van de Hulst, *Light scattering: by small particles*. Courier Dover Publications, 1957.

[15] L. Hu and G. Chen, "Analysis of optical absorption in silicon nanowire arrays for photovoltaic applications," *Nano Lett.*, vol. 7, no. 11, pp. 3249–3252, 2007.

[16] Y. Akahane, T. Asano, B.-S. Song, and S. Noda, "High-q photonic nanocavity in a two-dimensional photonic crystal," *Nature*, vol. 425, no. 6961, pp. 944–947, 2003.

[17] K. Seo, M. Wober, P. Steinvurzel, E. Schonbrun, Y. Dan, T. Ellenbogen, and K. B. Crozier, "Multicolored vertical silicon nanowires," *Nano Lett.*, vol. 11, no. 4, pp. 1851–1856, 2011.

[18] R. Sapienza, P. Garcia, J. Bertolotti, M. Martin, A. Blanco, L. Vina, C. López, and D. Wiersma, "Observation of resonant behavior in the energy velocity of diffused light," *Phys. Rev. Lett.*, vol. 99, no. 23, p. 233902, 2007.

[19] J. C. Hulteen and R. P. Van Duyne, "Nanosphere lithography: A materials general fabrication process for periodic particle array surfaces," *J. Vac. Sci. Technol. A*, vol. 13, no. 3, pp. 1553–1558, 1995.

[20] A. P. Suryavanshi, J. Hu, and M.-F. Yu, "Meniscus-controlled continuous fabrication of arrays and rolls of extremely long micro-and nano-fibers," *Adv. Mater.*, vol. 20, no. 4, pp. 793–796, 2008.

[21] P. J. Sazio, A. Amezcua-Correa, C. E. Finlayson, J. R. Hayes, T. J. Scheidemantel, N. F. Baril, B. R. Jackson, D.-J. Won, F. Zhang, E. R. Margine, *et al.*, "Microstructured optical fibers as high-pressure microfluidic reactors," *Science*, vol. 311, no. 5767, pp. 1583–1586, 2006.

[22] B. Tian, P. Xie, T. J. Kempa, D. C. Bell, and C. M. Lieber, "Single-crystalline kinked semiconductor nanowire superstructures," *Nat. Nanotechnol.*, vol. 4, no. 12, pp. 824–829, 2009.

[23] P. Caroff, K. Dick, J. Johansson, M. Messing, K. Deppert, and L. Samuelson, "Controlled polytypic and twin-plane superlattices in iii–v nanowires," *Nat. Nanotechnol.*, vol. 4, no. 1, pp. 50–55, 2008.

[24] H. Wang, C. S. Levin, and N. J. Halas, "Nanosphere arrays with controlled sub-10-nm gaps as surface-enhanced raman spectroscopy substrates," *J. Am. Chem. Soc.*, vol. 127, no. 43, pp. 14992–14993, 2005.

[25] H. Deniz, T. Khudiyev, F. Buyukserin, and M. Bayindir, "Room temperature large-area nanoimprinting for broadband biomimetic antireflection surfaces," *Appl. Phys. Lett.*, vol. 99, no. 18, pp. 183107–183107, 2011.

[26] P. Yang, "Nanotechnology: Wires on water," *Nature*, vol. 425, no. 6955, pp. 243–244, 2003.

[27] P. A. Smith, C. D. Nordquist, T. N. Jackson, T. S. Mayer, B. R. Martin, J. Mbindyo, and T. E. Mallouk, "Electric-field assisted assembly and alignment of metallic nanowires," *Appl. Phys. Lett.*, vol. 77, no. 9, pp. 1399–1401, 2000.

[28] B. D. Gates, Q. Xu, M. Stewart, D. Ryan, C. G. Willson, and G. M. Whitesides, "New approaches to nanofabrication: molding, printing, and other techniques," *Chem. Rev.*, vol. 105, no. 4, pp. 1171–1196, 2005.

[29] Y. Chen and A. Pepin, "Nanofabrication: Conventional and nonconventional methods," *Electrophoresis*, vol. 22, no. 2, pp. 187–207, 2001.

[30] D. Tsivion, M. Schvartzman, R. Popovitz-Biro, P. von Huth, and E. Joselevich, "Guided growth of millimeter-long horizontal nanowires with controlled orientations," *Science*, vol. 333, no. 6045, pp. 1003–1007, 2011.

[31] Z. Sun, E. Zussman, A. L. Yarin, J. H. Wendorff, and A. Greiner, "Compound core–shell polymer nanofibers by co-electrospinning," *Adv. Mater.*, vol. 15, no. 22, pp. 1929–1932, 2003.

[32] S. Dougherty and J. Liang, "Core–shell polymer nanorods by a two-step template wetting process," *Nanotechnology*, vol. 20, no. 29, p. 295301, 2009.

[33] W. Lu and C. M. Lieber, "Nanoelectronics from the bottom up," *Nat. Mater.*, vol. 6, no. 11, pp. 841–850, 2007.

[34] C. Thelander, P. Agarwal, S. Brongersma, J. Eymery, L. Feiner, A. Forchel, M. Scheffler, W. Riess, B. Ohlsson, U. Gösele, *et al.*, "Nanowire-based one-dimensional electronics," *Mater. Today*, vol. 9, no. 10, pp. 28–35, 2006.

[35] I. Brodie and J. J. Muray, *The physics of micro/nano-fabrication*. Springer, 1992.

[36] C. F. Bohren and D. R. Huffman, *Absorption and scattering of light by small particles*. Wiley. com, 2008.

[37] Y. Li, F. Qian, J. Xiang, and C. M. Lieber, "Nanowire electronic and optoelectronic devices," *Mater. Today*, vol. 9, no. 10, pp. 18–27, 2006.

[38] E. M. Freer, O. Grachev, X. Duan, S. Martin, and D. P. Stumbo, "High-yield self-limiting single-nanowire assembly with dielectrophoresis," *Nat. Nanotechnol.*, vol. 5, no. 7, pp. 525–530, 2010.

[39] P. W. Leu, R. S. Fearing, and A. Javey, "Nanowire active-matrix circuitry for low-voltage macroscale artificial skin,"

[40] A. Ziabicki, *Fundamentals of fibre formation: the science of fibre spinning and drawing*. Wiley, 1976.

[41] D. Li and Y. Xia, "Electrospinning of nanofibers: reinventing the wheel?," *Adv. Mater.*, vol. 16, no. 14, pp. 1151–1170, 2004.

[42] O. Ero-Phillips, M. Jenkins, and A. Stamboulis, "Tailoring crystallinity of electrospun plla fibres by control of electrospinning parameters," *Polymers*, vol. 4, no. 3, pp. 1331–1348, 2012.

[43] S. Y. Chou, P. R. Krauss, and P. J. Renstrom, "Nanoimprint lithography," *J. Vac. Sci. Technol. B*, vol. 14, no. 6, pp. 4129–4133, 1996.

[44] S. Y. Chou, P. R. Krauss, and P. J. Renstrom, "25-nanometer resolution," *Science*, pp. 85–87, 1996.

[45] T. Mårtensson, P. Carlberg, M. Borgström, L. Montelius, W. Seifert, and L. Samuelson, "Nanowire arrays defined by nanoimprint lithography," *Nano Lett.*, vol. 4, no. 4, pp. 699–702, 2004.

[46] M. Bayindir, F. Sorin, A. F. Abouraddy, J. Viens, S. D. Hart, J. D. Joannopoulos, and Y. Fink, "Metal–insulator–semiconductor optoelectronic fibres," *Nature*, vol. 431, no. 7010, pp. 826–829, 2004.

[47] M. Yaman, T. Khudiyev, E. Ozgur, M. Kanik, O. Aktas, E. O. Ozgur, H. Deniz, E. Korkut, and M. Bayindir, "Arrays of indefinitely long uniform nanowires and nanotubes," *Nat. Mater.*, vol. 10, no. 7, pp. 494–501, 2011.

[48] T. Khudiyev, E. Ozgur, M. Yaman, and M. Bayindir, "Structural coloring in large scale core–shell nanowires," *Nano Lett.*, vol. 11, no. 11, pp. 4661–4665, 2011.

[49] I. Donald, "Production, properties and applications of microwire and related products," *J. Mater. Sci.*, vol. 22, no. 8, pp. 2661–2679, 1987.

[50] J. J. Kaufman, G. Tao, S. Shabahang, E.-H. Banaei, D. S. Deng, X. Liang, S. G. Johnson, Y. Fink, and A. F. Abouraddy, "Structured spheres generated by an in-fibre fluid instability," *Nature*, vol. 487, no. 7408, pp. 463–467, 2012.

[51] S. Shabahang, J. Kaufman, D. Deng, and A. Abouraddy, "Observation of the plateau-rayleigh capillary instability in multi-material optical fibers," *Appl. Phys. Lett.*, vol. 99, no. 16, pp. 161909–161909, 2011.

[52] P. V. Braun, "Colour without colourants," *Nature*, vol. 472, no. 7344, pp. 423–424, 2011.

[53] C. E. Finlayson, P. Spahn, D. R. Snoswell, G. Yates, A. Kontogeorgos, A. I. Haines, G. P. Hellmann, and J. J. Baumberg, "3d bulk ordering in macroscopic solid opaline films by edge-induced rotational shearing," *Adv. Mater.*, vol. 23, no. 13, pp. 1540–1544, 2011.

[54] S. Robinson and R. Nakkeeran, "A bandpass filter based on 2d circular photonic crystal ring resonator," in *Wireless And Optical Communications Networks (WOCN), 2010 Seventh International Conference On*, pp. 1–3, IEEE, 2010.

[55] G. Westmacott, M. Frank, S. Labov, and W. Benner, "Using a superconducting tunnel junction detector to measure the secondary electron emission efficiency for a microchannel plate detector bombarded by large molecular ions," *Rapid Commun. Mass. Sp.*, vol. 14, no. 19, pp. 1854–1861, 2000.

[56] O. Jagutzki, V. Mergel, K. Ullmann-Pfleger, L. Spielberger, U. Spillmann, R. Dörner, and H. Schmidt-Böcking, "A broad-application microchannel-plate detector system for advanced particle or photon detection tasks: large area imaging, precise multi-hit timing information and high detection rate," *Nucl. Instrum. Meth. A*, vol. 477, no. 1, pp. 244–249, 2002.

[57] D.-I. Yeom, E. C. Mägi, M. R. Lamont, M. A. Roelens, L. Fu, and B. J. Eggleton, "Low-threshold supercontinuum generation in highly nonlinear chalcogenide nanowires," *Opt. Lett.*, vol. 33, no. 7, pp. 660–662, 2008.

[58] J. M. Dudley and J. R. Taylor, *Supercontinuum generation in optical fibers*. Cambridge University Press, 2010.

[59] T. Birks, W. Wadsworth, and P. S. J. Russell, "Supercontinuum generation in tapered fibers," *Opt. Lett.*, vol. 25, no. 19, pp. 1415–1417, 2000.

Appendix A

MATLAB Codes

Nano-sphere scattering efficiency estimation code

```
clear all;
clc;
m1=1.65;
m2=3.25;
nm=1*10^(-9);
a=100*nm;
b=a*1.33;
z=200*nm:5*nm:1000*nm;
for t=1:length(z)
clc;
x=2*pi*a/z(t);
y=2*pi*b/z(t);
An=(m2*m2*x*sqrt(pi/(2*m2*x))*besselj(0.5,m2*x)*m1*x
 *sqrt(pi/(2*m1*x))*(besselj(-0.5,x*m1)-besselj(1.5,x*m1))
 -m1*m1*x*sqrt(pi/(2*m1*x))*besselj(0.5,m1*x)*m2*x
 *sqrt(pi/(2*m2*x))*(besselj(-0.5,x*m2)-besselj(1.5,x*m2)))
 \(m2*(-m2)*x*sqrt(pi/(2*m2*x))*bessely(0.5,m2*x)*m1*x
 *sqrt(pi/(2*m1*x))*(besselj(-0.5,x*m1)-besselj(1.5,x*m1))
```

```
 -m1*m1*x*sqrt(pi/(2*m1*x))*besselj(0.5,m1*x)*(-m2)*x
 *sqrt(pi/(2*m2*x))*(bessely(-0.5,x*m2)-bessely(1.5,x*m2)));

Bn=(m2*m1*x*sqrt(pi/(2*m1*x))*besselj(0.5,m1*x)*m2*x
 *sqrt(pi/(2*m2*x))*(besselj(-0.5,x*m2)-besselj(1.5,x*m2))
 -m1*m2*x*sqrt(pi/(2*m2*x))*besselj(0.5,m2*x)*m1*x
 *sqrt(pi/(2*m1*x))*(besselj(-0.5,x*m1)-besselj(1.5,x*m1)))
 \((-m1)*(-m2)*x*sqrt(pi/(2*m2*x))*bessely(0.5,m2*x)*m1*x
 *sqrt(pi/(2*m1*x))*(besselj(-0.5,x*m1)-besselj(1.5,x*m1))
 +m2*m1*x*sqrt(pi/(2*m1*x))*besselj(0.5,m1*x)*(-m2)*x
 *sqrt(pi/(2*m2*x))*(bessely(-0.5,x*m2)-bessely(1.5,x*m2)));

an(1)=(abs((y*sqrt(pi/(2*y))*besselj(0.5,y)*(m2*y
 *sqrt(pi/(2*m2*y))*(besselj(-0.5,y*m2)-besselj(1.5,y*m2))
 -An*(-m2)*y*sqrt(pi/(2*m2*y))*(bessely(-0.5,y*m2)
 -bessely(1.5,y*m2)))-m2*y*sqrt(pi/(2*y))*(besselj(-0.5,y)
 -besselj(1.5,y))*(y*m2*sqrt(pi/(2*y*m2))*besselj(0.5,m2*y)
 -An*(-m2)*y*sqrt(pi/(2*m2*y))*bessely(0.5,m2*y)))
 /((y*sqrt(pi/(2*y)))*(besselj(0.5,y)+i*bessely(0.5,y))
 *(m2*y*sqrt(pi/(2*m2*y))*(besselj(-0.5,y*m2)-besselj(1.5,y*m2))
 -An*(-m2)*y*sqrt(pi/(2*m2*y))*(bessely(-0.5,y*m2)
 -bessely(1.5,y*m2)))-m2*y*sqrt(pi/(2*y))*((besselj(-0.5,y)
 -besselj(1.5,y))+i*((bessely(-0.5,y)-bessely(1.5,y))))
 *(y*m2*sqrt(pi/(2*y*m2))*besselj(0.5,m2*y)-An*(-m2)*y
 *sqrt(pi/(2*m2*y))*bessely(0.5,m2*y))))).^2;

bn(1)=(abs((m2*y*sqrt(pi/(2*y))*besselj(0.5,y)*(m2*y
 *sqrt(pi/(2*m2*y))*(besselj(-0.5,y*m2)-besselj(1.5,y*m2))
 -Bn*(-m2)*y*sqrt(pi/(2*m2*y))*(bessely(-0.5,y*m2)
 -bessely(1.5,y*m2)))-y*sqrt(pi/(2*y))*(besselj(-0.5,y)
 -besselj(1.5,y))*(y*m2*sqrt(pi/(2*y*m2))*besselj(0.5,m2*y)
 -Bn*(-m2)*y*sqrt(pi/(2*m2*y))*bessely(0.5,m2*y)))/
 ((m2*y*sqrt(pi/(2*y)))*(besselj(0.5,y)+i*bessely(0.5,y))
```

```
 *(m2*y*sqrt(pi/(2*m2*y))*(besselj(-0.5,y*m2)-besselj(1.5,y*m2))
 -Bn*(-m2)*y*sqrt(pi/(2*m2*y))*(bessely(-0.5,y*m2)
 -bessely(1.5,y*m2)))-y*sqrt(pi/(2*y))*((besselj(-0.5,y)
 -besselj(1.5,y))+i*((bessely(-0.5,y)-bessely(1.5,y))))
 *(y*m2*sqrt(pi/(2*y*m2))*besselj(0.5,m2*y)-Bn*(-m2)*y
 *sqrt(pi/(2*m2*y))*bessely(0.5,m2*y))))).^2;

for u=2:51

An=(m2*m2*x*sqrt(pi/(2*m2*x))*besselj(u-0.5,m2*x)*m1*x
 *sqrt(pi/(2*m1*x))*(besselj(u-1.5,x*m1)-besselj(u+0.5,x*m1))
 -m1*m1*x*sqrt(pi/(2*m1*x))*besselj(u-0.5,m1*x)*m2*x
 *sqrt(pi/(2*m2*x))*(besselj(u-1.5,x*m2)-besselj(u+0.5,x*m2)))
 \(m2*(-m2)*x*sqrt(pi/(2*m2*x))*bessely(u-0.5,m2*x)*m1*x
 *sqrt(pi/(2*m1*x))*(besselj(u-1.5,x*m1)-besselj(u+0.5,x*m1))
 -m1*m1*x*sqrt(pi/(2*m1*x))*besselj(u-0.5,m1*x)*(-m2)*x
 *sqrt(pi/(2*m2*x))*(bessely(u-1.5,x*m2)-bessely(u+0.5,x*m2)));

Bn=(m2*m1*x*sqrt(pi/(2*m1*x))*besselj(u-0.5,m1*x)*m2*x
 *sqrt(pi/(2*m2*x))*(besselj(u-1.5,x*m2)-besselj(u+0.5,x*m2))
 -m1*m2*x*sqrt(pi/(2*m2*x))*besselj(u-0.5,m2*x)*m1*x
 *sqrt(pi/(2*m1*x))*(besselj(u-1.5,x*m1)-besselj(u+0.5,x*m1)))
 \((-m1)*(-m2)*x*sqrt(pi/(2*m2*x))*bessely(u-0.5,m2*x)*m1*x
 *sqrt(pi/(2*m1*x))*(besselj(u-1.5,x*m1)-besselj(u+0.5,x*m1))
 +m2*m1*x*sqrt(pi/(2*m1*x))*besselj(u-0.5,m1*x)*(-m2)*x
 *sqrt(pi/(2*m2*x))*(bessely(u-1.5,x*m2)-bessely(u+0.5,x*m2)));

an(u)=(abs((y*sqrt(pi/(2*y))*besselj(u-0.5,y)*(m2*y
 *sqrt(pi/(2*m2*y))*(besselj(u-1.5,y*m2)-besselj(u+0.5,y*m2))
 -An*(-m2)*y*sqrt(pi/(2*m2*y))*(bessely(u-1.5,y*m2)
 -bessely(u+0.5,y*m2)))-m2*y*sqrt(pi/(2*y))*(besselj(u-1.5,y)
 -besselj(u+0.5,y))*(y*m2*sqrt(pi/(2*y*m2))*besselj(u-0.5,m2*y)
 -An*(-m2)*y*sqrt(pi/(2*m2*y))*bessely(u-0.5,m2*y)))
```

```
 /((y*sqrt(pi/(2*y)))*(besselj(u-0.5,y)+i*bessely(u-0.5,y))
 *(m2*y*sqrt(pi/(2*m2*y))*(besselj(u-1.5,y*m2)-besselj(u+0.5,y*m2))
 -An*(-m2)*y*sqrt(pi/(2*m2*y))*(bessely(u-1.5,y*m2)
 -bessely(u+0.5,y*m2)))-m2*y*sqrt(pi/(2*y))*((besselj(u-1.5,y)
 -besselj(u+0.5,y))+i*((bessely(u-1.5,y)-bessely(u+0.5,y))))
 *(y*m2*sqrt(pi/(2*y*m2))*besselj(u-0.5,m2*y)-An*(-m2)*y
 *sqrt(pi/(2*m2*y))*bessely(u-0.5,m2*y))))).^2;

bn(u)=(abs((m2*y*sqrt(pi/(2*y))*besselj(u-0.5,y)
 *(m2*y*sqrt(pi/(2*m2*y))*(besselj(u-1.5,y*m2)-besselj(u+0.5,y*m2))
 -Bn*(-m2)*y*sqrt(pi/(2*m2*y))*(bessely(u-1.5,y*m2)
 -bessely(u+0.5,y*m2)))-y*sqrt(pi/(2*y))*(besselj(u-1.5,y)
 -besselj(u+0.5,y))*(y*m2*sqrt(pi/(2*y*m2))*besselj(u-0.5,m2*y)
 -Bn*(-m2)*y*sqrt(pi/(2*m2*y))*bessely(u-0.5,m2*y)))/
 ((m2*y*sqrt(pi/(2*y)))*(besselj(u-0.5,y)+i*bessely(u-0.5,y))
 *(m2*y*sqrt(pi/(2*m2*y))*(besselj(u-1.5,y*m2)-besselj(u+0.5,y*m2))
 -Bn*(-m2)*y*sqrt(pi/(2*m2*y))*(bessely(u-1.5,y*m2)
 -bessely(u+0.5,y*m2)))-y*sqrt(pi/(2*y))*((besselj(u-1.5,y)
 -besselj(u+0.5,y))+i*((bessely(u-1.5,y)-bessely(u+0.5,y))))
 *(y*m2*sqrt(pi/(2*y*m2))*besselj(u-0.5,m2*y)-Bn*(-m2)*y
 *sqrt(pi/(2*m2*y))*bessely(u-0.5,m2*y))))).^2;

an(u)=an(u)+an(u-1);
bn(u)=bn(u)+bn(u-1);

end;
an(t)=an(u);
bn(t)=bn(u);
q(t)=2*(an(t)+bn(t))./x;
end;
figure
plot(z,q);
```

Nano-wire scattering efficiency estimation code

TM case

```
clear all;
clc;
m1=1.65;
m2=3.25;
nm=1*10^(-9);
a=150*nm;
b=a*1.5;
z=200*nm:5*nm:1000*nm;
for t=1:length(z)
clc;
x=2*pi*a/z(t);
y=2*pi*b/z(t);
J=m2*besselj(0,x*m2)-(m2^3/m1^2)*besselj(0,x*m1)*(besselj(-1,x*m2)
 -besselj(1,x*m2))/(besselj(-1,x*m1)-besselj(1,x*m1));

Y=(m2^3/m1^2)*besselj(0,x*m1)*(bessely(-1,x*m2)-bessely(1,x*m2))
 /(besselj(-1,x*m1)-besselj(1,x*m1))-m2*bessely(0,x*m2);

C=m2*besselj(0,y*m2)+m2*(J/Y)*(bessely(0,y*m2));
D=(m2^3)*(besselj(-1,y*m2)-besselj(1,y*m2))+(m2^3)*(J/Y)*
 (bessely(-1,y*m2)-bessely(1,y*m2));

bn(1)=(abs((C*(besselj(-1,y)-besselj(1,y))-besselj(0,y)*D)
 /(C*(besselh(-1,y)-besselh(1,y))-besselh(0,y)*D))).^2;

for u=2:51
J=m2*besselj(u-1,x*m2)-(m2^3/m1^2)*besselj(u-1,x*m1)*(besselj(u-2,x*m2)
 -besselj(u,x*m2))/(besselj(u-2,x*m1)-besselj(u,x*m1));

Y=(m2^3/m1^2)*besselj(u-1,x*m1)*(bessely(u-2,x*m2)-bessely(u,x*m2))
```

```
 /(besselj(u-2,x*m1)-besselj(u,x*m1))-m2*bessely(u-1,x*m2);

C=m2*besselj(u-1,y*m2)+m2*(J/Y)*(bessely(u-1,y*m2));
D=(m2^3)*(besselj(u-2,y*m2)-besselj(u,y*m2))+(m2^3)*(J/Y)
 *(bessely(u-2,y*m2)-bessely(u,y*m2));

bn(u)=bn(u-1)+2*(abs((C*(besselj(u-2,y)-besselj(u,y))-besselj(u-1,y)*D)
 /(C*(besselh(u-2,y)-besselh(u,y))-besselh(u-1,y)*D))).^2;

end;
bn(t)=bn(u);
q(t)=2*bn(t)./x;
end;
figure
plot(z,q);
```

TE case

```
clear all;
clc;
m1=1.65;
m2=3.25;
nm=1*10^(-9);
a=150*nm;
b=a*1.5;
z=200*nm:5*nm:1000*nm;
for t=1:length(z)
clc;
x=2*pi*a/z(t);
y=2*pi*b/z(t);
J=m1*m2*besselj(0,x*m1)*(besselj(-1,x*m2)-besselj(1,x*m2))
 -m2*m1*besselj(0,x*m2)*(besselj(-1,x*m1)-besselj(1,x*m1));
```

```
Y=m2*m1*bessely(0,x*m2)*(besselj(-1,x*m1)-besselj(1,x*m1))
 -m1*m2*besselj(0,x*m1)*(bessely(-1,x*m2)-bessely(1,x*m2));

D=(m2^2)*(Y/J)*besselj(0,y*m2)+(m2^2)*(bessely(0,y*m2));
C=(m2^2)*(Y/J)*(besselj(-1,y*m2)-besselj(1,y*m2))
 +(m2^2)*(bessely(-1,y*m2)-bessely(1,y*m2));

an(1)=(abs((D*(besselj(-1,y)-besselj(1,y))-besselj(0,y)*C)
 /(D*(besselh(-1,y)-besselh(1,y))-besselh(0,y)*C))).^2;

for u=2:51
J=m1*m2*besselj(u-1,x*m1)*(besselj(u-2,x*m2)-besselj(u,x*m2))
 -m2*m1*besselj(u-1,x*m2)*(besselj(u-2,x*m1)-besselj(u,x*m1));

Y=m2*m1*bessely(u-1,x*m2)*(besselj(u-2,x*m1)-besselj(u,x*m1))
 -m1*m2*besselj(u-1,x*m1)*(bessely(u-2,x*m2)-bessely(u,x*m2));

D=(m2^2)*(Y/J)*besselj(u-1,y*m2)+(m2^2)*(bessely(u-1,y*m2));
C=(m2^2)*(Y/J)*(besselj(u-2,y*m2)-besselj(u,y*m2))+(m2^2)
 *(bessely(u-2,y*m2)-bessely(u,y*m2));

an(u)=an(u-1)+2*(abs((D*(besselj(u-2,y)-besselj(u,y))-besselj(u-1,y)*C)
 /(D*(besselh(u-2,y)-besselh(u,y))-besselh(u-1,y)*C))).^2;
end;
an(t)=an(u);
q(t)=2*an(t)./x;
end;
figure
plot(z,q);
```